ZnTe Nanostructural Synthesis for Electronic and Optoelectronic Devices

by

Jhih-hong Peng

A Dissertation Presented in Partial Fulfillment
of the Requirements for the Degree
Doctor of Philosophy

Approved July 2017 by the
Graduate Supervisory Committee:

Hongbin Yu, Chair
Ronald Roedel
Michael Goryll
Yuji Zhao

ARIZONA STATE UNIVERSITY

August 2017

ABSTRACT

Zinc telluride (ZnTe) is an attractive II-VI compound semiconductor with a direct bandgap of 2.26 eV that is used in many applications in optoelectronic devices. Compared to the two dimensional (2D) thin-film semiconductors, one-dimensional (1D) nanowires can have different electronic properties for potential novel applications. In this work, we present the study of ZnTe nanowires (NWs) that are synthesized through a simple vapor-liquid-solid (VLS) method. By controlling the presence or the absence of Au catalysts and controlling the growth parameters such as growth temperature, various growth morphologies of ZnTe, such as thin films and nanowires can be obtained. The characterization of the ZnTe nanostructures and films was performed using scanning electron microscope (SEM), energy-dispersive X-ray spectroscopy (EDX), high- resolution transmission electron microscope (HRTEM), X-ray diffraction (XRD), photoluminescence (PL), Raman spectroscopy and light scattering measurement. After confirming the crystal purity of ZnTe, two-terminal diodes and three-terminal transistors were fabricated with both nanowire and planar nano-sheet configurations, in order to correlate the nanostructure geometry to device performance including field effect mobility, Schottky barrier characteristics, and turn-on characteristics. Additionally, optoelectronic properties such as photoconductive gain and responsivity were compared against morphology. Finally, ZnTe was explored in conjunction with ZnO in order to form type-II band alignment in a core-shell nanostructure. Various characterization techniques including scanning electron microscopy, energy-dispersive X-ray spectroscopy , x-ray diffraction, Raman spectroscopy, UV-vis reflectance spectra and photoluminescence were used to investigate the modification of ZnO/ZnTe core/shell structure properties. In PL spectra, the eliminated PL intensity of ZnO wires is primarily attributed to the efficient charge transfer process occurring between ZnO and ZnTe, due to the band alignment in the core/shell struc-

ture. Moreover, the result of UV-vis reflectance spectra corresponds to the band gap energy of ZnO and ZnTe, respectively, which confirm that the sample consists of ZnO/ZnTe core/shell structure of good quality.

DEDICATION

To my parents, my wife, and my 3 children.

ACKNOWLEDGMENTS

I would like to express my sincere gratitude to my advisor, Professor Hongbin Yu, for his support, guidance and patience during my research. My special thanks to the dissertation committee members, Professor Ronald Roedel, Professor Michael Goryll, and Professor Yuji Zhao for their helpful suggestions and for serving on my dissertation committee. I am also thankful for Professor Sandwip K Dey's financial support and the use of facilities in LeRoy Eyring Center for Solid State Science. Particular thanks to my research group members: Dr. Xiao Di Sun Zhou, and Ebraheem Ali Azhar.

TABLE OF CONTENTS

CHAPTER Page

LIST OF TABLES

LIST OF FIGURES

Figure Page

Figure Page

Figure Page

Figure Page

Chapter 1

INTRODUCTION

1.1 Motivation

1.1.1 Energy Challenges

The erratic economics that govern energy supply are based upon the notion that gas and other liquified energy is undeniably a finite resource and its accessibility is at the mercy of external effects, such as exponentially increasing consumer demand, and exponentially decreasing supply, due in some part by speculative political unrest. Additionally, the recent exit of the United States from the Paris Climate Accord has spurred a tremendous amount of innovation over new energy resources and technologies (Foley *et al.*, 2017). As a result, these factors have motivated the scientific community has taken upon the enormous challenge of exploring novel, cleaner, and more renewable sources of energy. While there is a strong commercial motivation for shifted focus on alternative energy, this shift is also demonstrated in academic pursuits.

1.1.2 Nanowire Photovoltaics

Materials systems for various energy harvesting schemes such as piezo-electric materials (Kong and Wang, 2003) or those used for water-splitting (Van de Krol *et al.*, 2008) to create hydrogen fuel cells, have received wide attention, but are unparalleled to the growth of interest in photovoltaics. "Back of the envelope" calculations have demonstrated that harvesting the total energy from only one hour of complete solar radiation would be enough to power the world's energy consumption for a day (Kayes

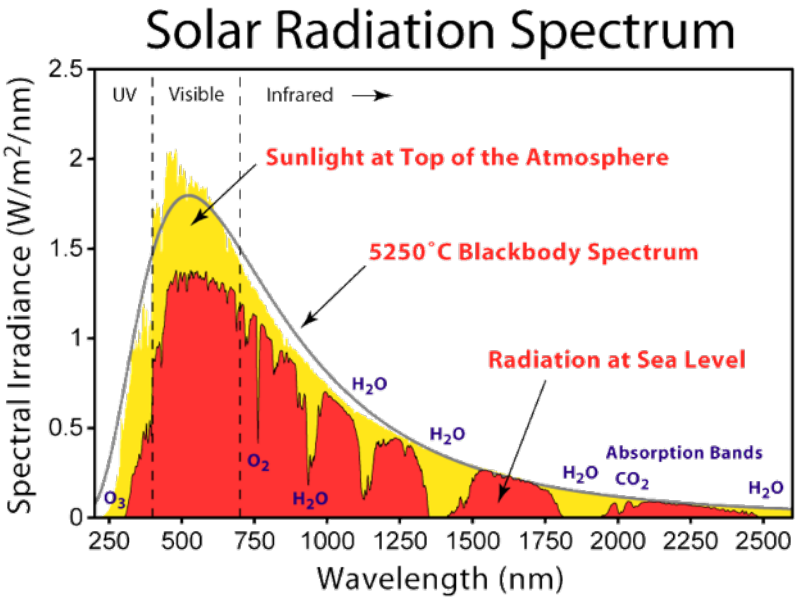

Figure 1.1: Solar Spectrum of one sun at Air Mass 1.5

et al., 2005). However, therein lies an inherent challenge of finding a system that can effectively capture the energy from the entire solar spectrum, illustrated in Figure 1.1. Because of quantized band edge transitions from homogenous semiconducting materials and equivalent pn-junctions, no single material can accomplish the task of converting the entire solar spectrum into usable energy. A number of photovoltaic material systems have emerged within the past few decades, including multijunction cells, nanostructure cells, and organics. The relative performance and evolution of progress throughout the years. Conversion and external quantum efficiency are, however, not the only metrics which determine a successful photovoltaic material. While the efficiency of single crystal silicon and multijunction cells seems to indicate staggering performance, the limiting tradeoffs that stop consumer level production are the astounding cost and difficulty to fabricate and grow (Kayes *et al.*, 2005; Hu and Chen, 2007). Organics suffer from low operation lifetimes due to the polymer layers which are prone to oxidation (Schrier *et al.*, 2007). This leaves a variety of thin film and nonmaterial technologies which are hopeful options toward low cost of produc-

tion, lower cost per raw material (due to greater abundance) and higher performance than current crystal technologies. This is especially true of oxide materials which are chemically stable, lack toxicity, and are incredibly abundant. Additionally, nanowire structures, in particular, offer a number of inherent advantages that set apart from other traditional photovoltaic technologies (Hochbaum and Yang, 2009).

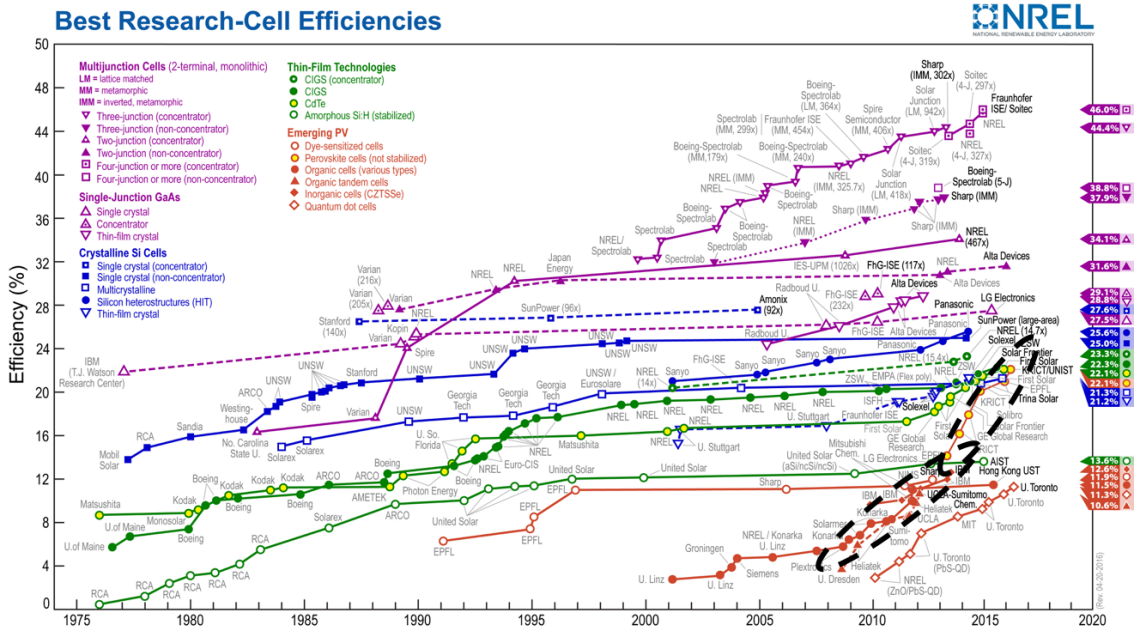

Figure 1.2: Evolution of photovoltaic material systems and power conversion efficiency measures across the last century (from NREL)

Nanowires offer a large surface-to-volume ratio for effective chemical and catalytic reactions and a large number of surface states to minimize dark current (current level with no illumination). Nanowires are not limited by their growth substrate because they have higher tolerance to lattice mismatching, allowing the use of low cost and amorphous substrates (which also proves to be useful in the formation of heterostructures) (Soci *et al.*, 2007a). Nanowires in a vertical array formation have very much improved light trapping mechanisms which are very advantageous for light absorption, a key component needed for photovoltaics. This configuration enhances light absorption simply because of the waveguiding effect which reduces surface reflectance and

minimizes angular dependence (Kayes *et al.*, 2005). The mechanism and performance of charge generation/separation in heterogeneous nanowires is also advantageous for photovoltaic design, however the mechanism for charge collection limits its performance, especially in axially oriented heterojunctions. For heterostructure materials, the different compositions of different semiconducting materials indicates different effective masses for electrons and holes, which in turn gives rise to a quasielectric field for the carriers. For a Type II staggering band alignment, the charge separation suppresses intrinsic recombination at the junction without the need for additional doping (Capasso, 1986; Wang *et al.*, 2008). On the other hand, charge collection, or transportation, is plagued by recombination which occurs at the surface, interface, or at bulk defects. Because of the inherently large surface to volume ratio of nanowires, surface recombination remains a major challenge to overcome (Bae *et al.*, 2010). Radially oriented, or core/shell heterostructure nanowires offer advantages very distinct from the axially oriented heterostructure, which are illustrated in Figure 1.3. First, the junction interface extends along the length of the nanowire, maximizing interface area6. Secondly, because the radial configuration produces orthogonal pathways for light absorption and carrier collection, a carrier collection distance can be made comparable or even smaller than the minority carrier diffusion length. This suggests that photogenerated carriers can reach the p/n regions or electrodes of the surrounding geometry with high efficiency and low bulk recombination (Hu and Chen, 2007). This is in stark contrast to planar solar cells which are limited by unwanted recombination.

1.2 II-IV Nanowires

Compound II-VI semiconducting nanowires can be produced at relatively low costs, either by solution or thermal methods. This has increased interest, in the past years of developing II-VI compound nanowire photovoltaics. These materials enjoy

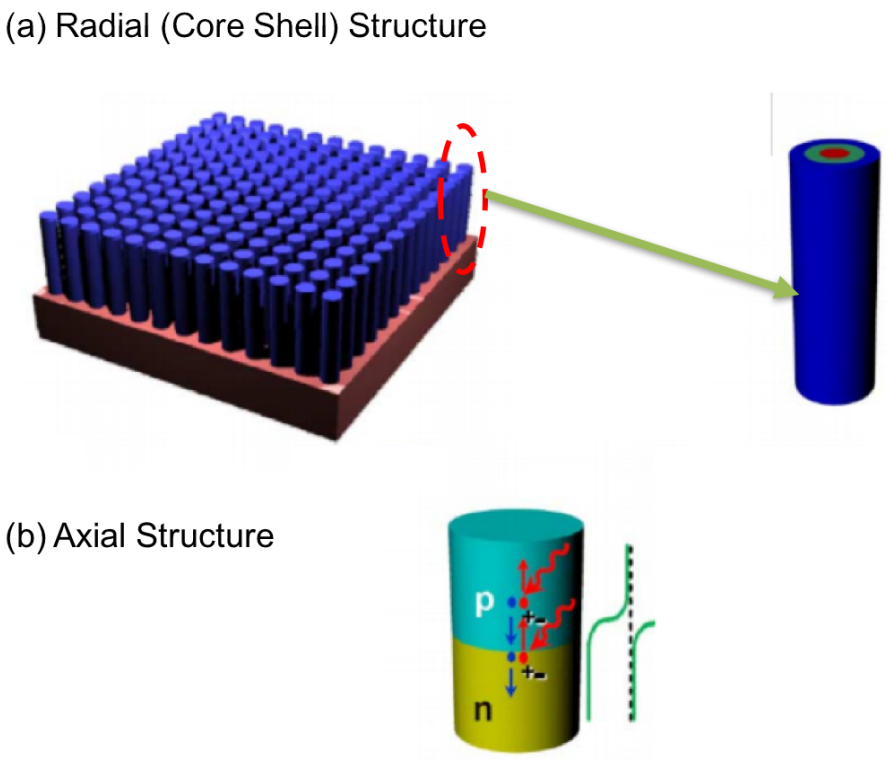

Figure 1.3: Comparison of (a) radial and (b) axial nanowire photovoltaic heterostructures

some intrinsic advantages found within most inorganic materials such as high carrier mobility, robust material stability, and high interfacial area (Schrier *et al.*, 2007). Unfortunately, II-VI materials are limited by their native defects and controlled doping is still considered such a challenging milestone (Desnica, 1998). The use of II-VI nanowires in conjunction with semiconducting dyes or organic polymers for fabrication of hybrid solar cells may substantially increase the efficiency and viability of these materials.

ZnO nanowires are the most researched metal oxide semiconductors and have received a great deal of attention due to ease of growth, rich optical, electrical, and mechanical properties, and a promising variety of applications. The problem however, is its band gap (3.37 eV) which limits the absorption of light illuminated on ZnO to the

UV spectrum, and to date, the best theoretical calculations of photovoltaic efficiency are 7% while having only experimentally been shown to accomplish 2% (Torchynska and Polupan, 2002). However, ZnO is highly conductive and intrinsically n-type and in a nanowire geometry, a large junction area and contact area can be used for electron collection, as previously described (Wang *et al.*, 2008).

Many techniques have been employed toward using smaller band gap materials to expand the absorbance, which allows for increased light harvesting and overall energy-conversion efficiency of the solar cell. One of the most popular methods is to fabricate a core/shell structure by coating ZnO NWs with a uniform thin film shell of the II-VI group of materials (Leschkies *et al.*, 2007; Tak *et al.*, 2009). The core/shell type-II heterojunction between the ZnO nanowire rod and the semiconducting surrounding lead to effective charge separation with the shell acting as an absorber or generation site and the nanowire core as an electron transporter (Leschkies *et al.*, 2007; Lévy-Clément *et al.*, 2005). Type-II core/shell heterostructure configurations provide the advantage of broadening the absorbed solar spectrum through weak interfacial transitions (Leschkies *et al.*, 2007) and increase the carrier lifetime due to slow electron-hole recombination in the spatially charge separated region (Kim *et al.*, 2003) and minimize radiative recombination losses (Zhang *et al.*, 2008c). However, for effective transport of electrons in the ZnO core, and holes in the shell, it is important to be able to adjust the thickness of the cell to maximize generation of the charge pairs while maintaining effective transport. Some simulation and experimental work in this area has been explored via the use of selenide (Bouazzi *et al.*, 1978), sulfide (Goto *et al.*, 2009), and telluride (Schrier *et al.*, 2007) as a shell material.

1.3 Literature Review

A review of the literature in regards to ZnTe nanostructures for electronic and optoelectronic applications is presented as follows.

1.3.1 ZnTe Thin Film and Nanostructural Synthesis

ZnTe thin film and nanostructures have had reported synthesis techniques that range from molecular beam epitaxy (MBE) (Bozzini *et al.*, 2000), electrodeposition (Bacaksiz *et al.*, 2009), metal-organic chemical vapor deposition (MOCVD) (Amutha *et al.*, 2006), thermal evaporation (Tanaka *et al.*, 2009a), sputtering (Spath *et al.*, 2005a), and solvothermal synthesis (Du *et al.*, 2006). Among these, the technique of thermal evaporation has been among the most reported due to the ability to deposit ZnTe conformally and as a blanket whole, over a large surface, with extreme facility. While able to produce highly uniform and crystallographically pure ZnTe, MBE suffers from a large cost with low throughput and makes large scale commercialization difficult (Bozzini *et al.*, 2000). Techniques involving solution-based synthesis, while potentially cost-effective, present difficulties with producing ZnTe that are stochiometrically pure (due to residual solvent and other impurities), and further pose difficultues with integrating synthesis directly with processing (Du *et al.*, 2006). Among these, vapor deposition has shown to trades off with some of these limitations by forming high quality crystals, with larger throughput, at lower cost.

Devami et al produced a comprehensive model that attempted to correlate morphological structure of synthesized ZnTe with temperature and content percentage. They were able to demonstrate how maximal length and tapering could be achieved and largely attributed the variation to the diffusion coefficient of the source ZnTe vapor. They also noted that the thickness of gold film catalyst largely affected diameter

and therefore thickness of two-dimensional ribbon structures. Figure 1.4 summarizes these findings.

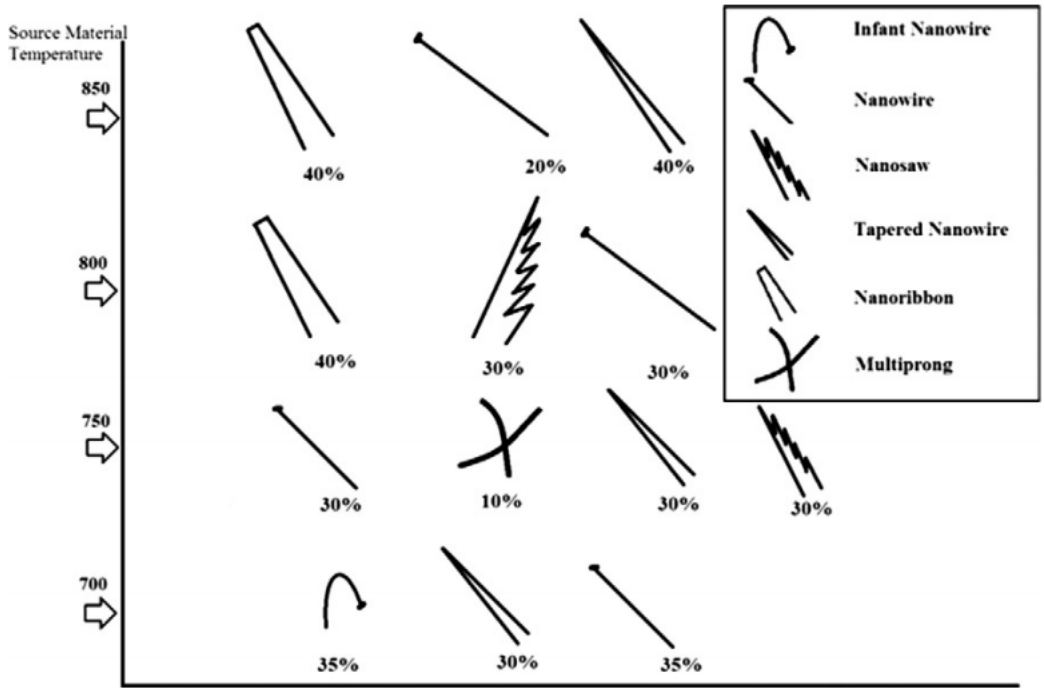

Figure 1.4: Schematic of nanostructures grown with different source material temperatures and their approximate percentage. Other conditions are 300 Torr, substrate heater at 500 °C, 25 sccm argon flow (from Devami et al.)

1.3.2 ZnTe Nanostructures for Electronic and Optoelectronic Devices

The study of channel conductance and photoconductive properties was undertaken by many researchers using 1D ZnTe materials. Doped and undoped ZnTe films have traditionally been used to realize a variety of optoelectronic devices such as photodetectors (Chang *et al.*, 2001) and intermediate solar cell layers (Gessert *et al.*, 2009; Rioux *et al.*, 1993; Spath *et al.*, 2005b). Additionally, ZnTe has often been compared to GaAs and ZnS systems in regards to its superior electro-optical coefficient and electron-LO-phonon (polaron) coupling constant (Kumagai and Kobayashi, 2012; Pelekanos *et al.*, 1991; Kaminow and Turner, 1966; Xue and Zhang, 1997), as

well as GaN/InGaN emitters for circumventing the problem of phase segregation in compositional band edge engineering (Osamura *et al.*, 1975; Moon *et al.*, 2001). ZnTe nanowires has led to the successful fabrication of field effect transistors (Cao *et al.*, 2012; Huo *et al.*, 2006a; Li *et al.*, 2010a, 2011a; Liu *et al.*, 2013a; Wu *et al.*, 2012) and photodetectors (Zhang *et al.*, 2008a; Liu *et al.*, 2013a). Figure 1.5 illustrates the earliest reports of two-terminal and three-terminals devices composed of ZnTe nanowires (Cao et al.).

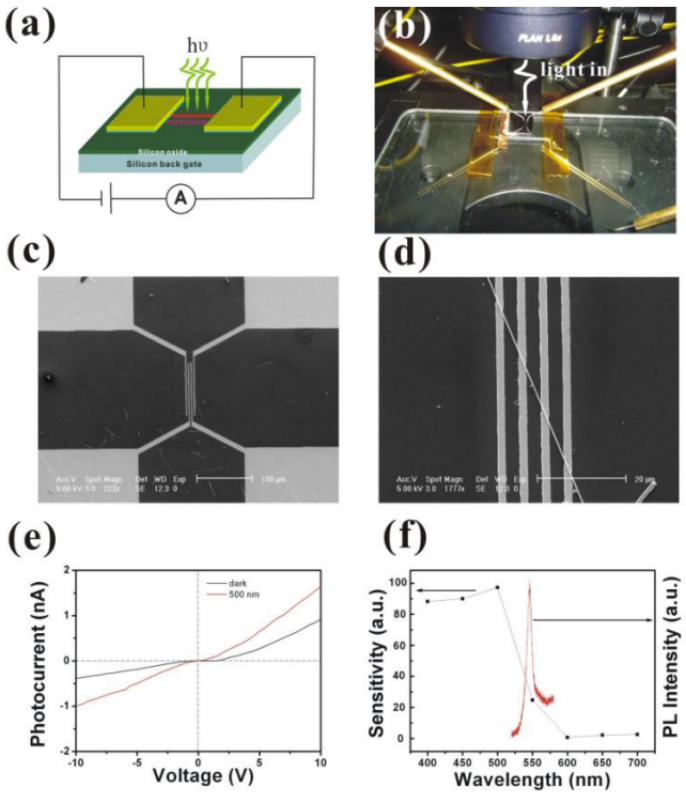

Figure 1.5: A schematic illustration of an individual ZnTe nanowire configured as a photodetector. (b) Photoconductivity measurement of a ZnTe nanowire device on a SiO2/Si substrate. (c) A representative low-magnification and (d) high-magnification SEM image of a single-crystalline ZnTe nanowire device. (e) Comparative I-V characteristics of the ZnTenanowire photodector illuminated with a light of 400 and 500 nm wavelength and under dark conditions. (f) Spectral response (left) of the nanowire measured at a constant bias voltage of 10 V. The normalized room-temperature PL spectrum (right) of the ZnTe nanowires is also illustrated (from Cao et al.)

1.3.3 ZnO/ZnTe Core Shell Photodiodes

Experimental demonstrations of ZnO/ZnS and ZnO/ZnTe were found in conjunction to the above theory work. In the case of ZnS (Wang *et al.*, 2010), a vertically aligned ZnO/ZnS core/shell nanowire array with type II band alignment was directly synthesized on an indium-tin-oxide glass substrate and the photovoltaic effect of the nanowire array was investigated. The report indicates that ZnS coating is found to quench the photoluminescence of ZnO nanowires but enhance the photocurrent with faster response in the photovoltaic device, indicating improvement in charge separation and collection in the type-II core/shell nanowire. While their work seems to suggest a photovoltaic effect, no numerical reports of photovoltaic parameters such as open circuit voltage, short circuit current, nor efficiency were reported. For ZnO/ZnTe (Zheng *et al.*, 2010) structures, large area, well-aligned type-II nanowire arrays were fabricated on sapphire substrate. Luo et al most recently formed ZnO/ZnTe core shell structures with a process flow described in Figure 1.7 and the proposed band alignment is shown in Figure 1.6. The ZnO nanowires were grown in a furnace by chemical vapor deposition and then were coated with a ZnTe shell on the ZnO nanowires surface by a metal-organic chemical deposition chamber. The morphology and size distribution of the ZnO/ZnTe core-shell nanowire arrays were studied by scanning electron microscopy (SEM) and the crystal structure was examined by x-ray diffraction (XRD). Transmission measurement was used to study the optical properties of the core-shell nanowires. The results indicated that the ZnO/ZnTe core-shell nanowire arrays have good crystalline quality. The report further indicates that the nanowire arrays have good light absorption characteristics making it suitable for making photovoltaic applications. However as in the ZnS case, no actual measures were taken to fabricating a standard solar cell and the important figures of merit charac-

terizing the cell were certainly not measured. This is probably an indication that the experimental performance of these devices is currently very poor. While the reports of ZnTe are very few and far between, there are in fact many ZnO/ZnS reports but they all seem to be permutations of the same report, delivering no useful photovoltaic parameters. This seems to suggest that much experimental work needs to be done in order to reach the predicted levels of simulations, worthy of publication.

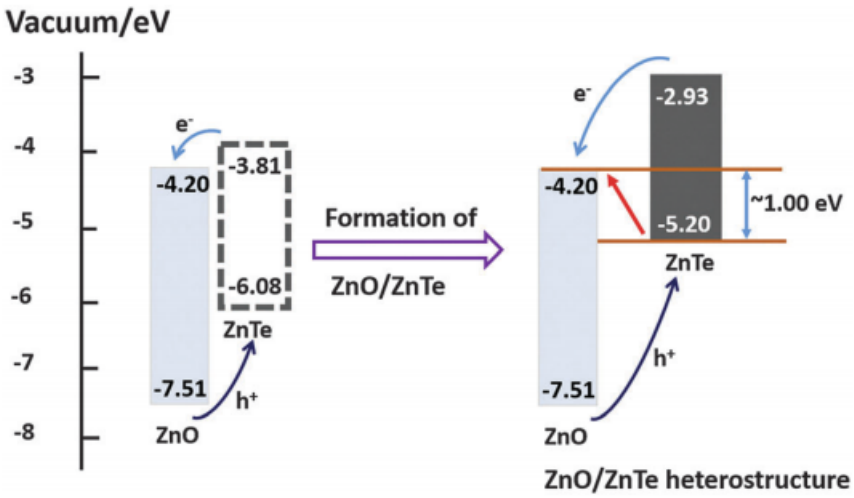

Figure 1.6: Band alignment modification upon the formation of a ZnO/ZnTe heterostructure and the corresponding charge transfer process upon illumination (from Luo et al.)

1.4 Research Goals

1.4.1 ZnTe for Electronic and Optoelectronic Applications

ZnTe has been demonstrated in a variety of applications, and serves as a fundamental semiconduting material to achieve these ends. There are still several obstacles that stand in the way of any form of ZnTe usage in microelectronic and solar cell applications. The first includes controlled morphological and electronic properties from source materials and synthesis conditions. The second includes optimization of these

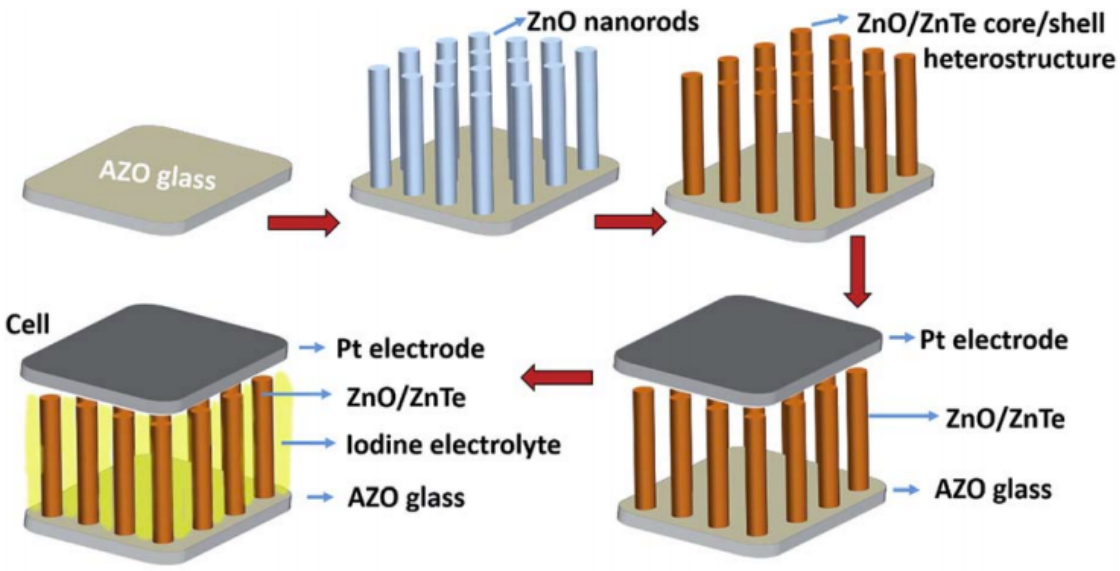

Figure 1.7: Process flow of preparing the vertically aligned ZnO/ZnTe heterostructure based solar cell. There is a transparent hot-melt ring between Pt counter electrode and ZnO/ZnTe based photoanode (from Luo et al.)

physical and chemical properties toward better electronic and optoelectronic performance. Lastly, it is important to understand how ZnTe can be incorporated to modify ZnO nanowires for a type-II band alignment, for potential solar cell applications.

1.4.2 Objectives

This study aims to focus on:

- High temperature vapor phase transport for high quality ZnTe nanostructures and controlled morphology
- Evaluation of nanostructured geometry in relation to electronic and optoelectronic performance
- Integration of ZnTe in vertical ZnO nanowire arrays for type-II band alignment

1.4.3 Research Approach

This work aims to answer a set of questions leading to an overall understanding of ZnTe nanostrucutures. A summary of some of these findings is discussed as follows:

- Chapter 2
  - Hypothesis: The use of catalyst and the variation of growth temperature can significantly affect the kind of ZnTe nanostructure that emerges
    - *Observation 1*: The presence of catalyst forms nanostructures including nanowires and nanosheets.
      - *Experimental Design*: A synthesis of ZnTe was undertaken with Au catalyst
      - *Fundamental Physical Interactions Uncovered*: ZnTe undergoes vapor-liquid-solid growth mechanism during formation to create a eutectic that facilitates aligned growth.
    - *Observation 2*: Growth temperature has a strong influence over
      - *Experimental Design*: ZnTe was grown in a single zone furnace capable of producing multiple temperatures in a single growth trial.
      - *Fundamental Physical Interactions Uncovered*: ZnTe undergoes a scaffolding and filling effect that creates 2D sheets from a single ZnTe wire.
- Chapter 3
  - Hypothesis: ZnTe nanomaterial geometry has no significant difference in electrical and optoelectronic performance responses.
    - *Observation 1*: Field effect mobility, subthreshold swing, and contact barrier found to be larger for ZnTe nanosheets, as compared to ZnTe nanowires
      - *Experimental Design*: IV characteristics across ZnTe nano-geometry (categories), for varying gate voltages (numerical ratio scale).
      - *Fundamental Physical Interactions Uncovered*: Conformal and intimate contact between ZnTe nanosheets and gate oxide. NWs have a single line conduction path with a larger density of surface oxygen states impeding transport.
    - *Observation 2*: Nanowires exhibit larger photoconductive gain than nanosheets
      - *Experimental Design*: IV measurements under different illumination power density (ratio scale), across two geometries (categorical).
      - *Fundamental Physical Interactions Uncovered*: Smaller power exponent of maximum current relation (for nanowires) indicates a greater abundance of trap states, from surface oxygen formation. Larger surface to volume ratio of nanowires magnifies this effect.

- Chapter 4
  - Hypothesis: ZnTe can conformally cover ZnO nanowire arrays
    - *Observation*: ZnTe conformally covers ZnO nanowire arrays
      - *Experimental Design*: ZnTe growth was undertaken on ZnO nanowire array
      - *Fundamental Physical Interactions Uncovered*: ZnTe covers ZnO at the reaction limited regime such that it blankets ZnO wires without forming into secondary substructures

1.4.4 Merit

This work is important because ZnTe is a robust material and capable of realizing advanced solar cell technology. This study aims to inform future generations of ZnTe nanostructure researchers of the variety of considerations and pitfalls that may emerge when studying ZnTe. ZnTe has been described as a highly promising material for commercialization, and yet many road-blocks exist within realizing it on such an industrial scale. While this work does not necessarily "move mountains" in terms of influencing industries committed to their own set of materials and workflow, it will inform the general public of what the material is capable of achieving.

1.5 Organization of the dissertation

The organization of this dissertation is such that the Chapter 2 discusses the synthesis of ZnTe including the use of catalyst and modulation of growth temperature to create thin films and nanostructures. Chapter 3 discusses the fabrication of ZnTe devices and how the morphological structure affects functional performance. Chapter 4 discusses ZnO/ZnTe core/shell nanostructures. Chapter 5 concludes this dissertation.

Chapter 2

FROM POLY-CRYSTALLINE THIN FILMS TO SUBMICRON STRUCTURES: MORPHOLOGICAL EVOLUTION OF ZNTE THROUGH CATALYST CONTROL

2.1 Abstract

Zinc Telluride (ZnTe) poly-crystalline thin films and submicron, single-crystal features (wires and sheets) were synthesized by a vapor deposition technique. The morphology of grown structures were controlled through the absence and the presence of gold (Au) catalyst deposited as a seeding layer atop substrates prior to growth. As the growth temperature increased from 349 °C to 562 °C, the grain sizes of poly-crystalline thin films increased from an average of 1.12 μm to 4.35 μm. Coupled with X-ray diffraction (XRD) analysis, the Williamson-Hall model was employed to discern a reduction of microstrain leading to increased crystallite size. Furthermore analysis of grain size as a function of growth temperature indicate an increase of grain boundary mobility with increased grain size. For nanostructures, field emission scanning electron microscopy (FESEM) reveals a variety of morphological features from single-dimensional wires to two-dimensional sheets. High-resolution transmission electron microscopy (HR-TEM) and XRD of the ZnTe nanostructures reveal single-crystallinity, with a moderate preference for the (111) growth orientation due to lower surface energy. Strong band edge emission from photoluminescence (PL) and absorption from light scattering of ZnTe nanostructures was observed and the intensity ratio of the band edge peak to the O_2 defect related peak (550 nm/725 nm) increases with the growth temperature, indicating the suppression of unintended oxygen-related defects.

2.2 Introduction

Wide band gap II-VI semiconductors have been studied extensively due to interests in potential applications from modifying fundamental crystal structure as related to electrical, and optical properties (Jie *et al.*, 2010). Among them, Zinc Telluride (ZnTe) is an attractive compound semiconductor with a direct band gap of 2.26 eV at room temperature (Garcia *et al.*, 2001), and exhibits a cubic, zinc blende lattice structure. ZnTe has been integrated in several optoelectronic device applications including light-emitting diodes (LEDs), laser diodes (LDs), photodetectors, and solar cells (Tanaka *et al.*, 2009b; Liu *et al.*, 2013b; Fan *et al.*, 2011; Gunshor *et al.*, 1996). ZnTe typically exhibits p-type conductivity due to self-compensation (Zhang *et al.*, 2008a; Li *et al.*, 2010b, 2011a), and is therefore a choice material in forming p-n heterojunction diodes with preferentially n-type semiconductors (Reiss *et al.*, 2009).

ZnTe has been reportedly grown from several techniques including molecular beam epitaxy (MBE), electrodeposition, metal-organic chemical vapor deposition (MOCVD), thermal evaporation, sputtering, and solvothermal synthesis (Bozzini *et al.*, 2000; Bacaksiz *et al.*, 2009; Shan *et al.*, 2002; Amutha *et al.*, 2006; Tanaka *et al.*, 2009a; Spath *et al.*, 2005a; Du *et al.*, 2006). Thermal evaporation is the most commonly employed method for synthesizing ZnTe thin films due to its simplicity of blanket deposition onto large surface area. MBE, while highly pure and highly uniform, suffers from high cost and low throughput and making commercialization and mass production difficult. Solution-based techniques pose difficulties in device fabrication, due to the complexity of integrating synthesis directly into the processing sequence. Furthermore, ZnTe nanostructures formed by solution-based techniques typically yield smaller lengths and correspondingly smaller aspect ratios. Solution based techniques also tend to produce lower crystal quality due to residual solvent

and impurities (Du *et al.*, 2006). Vapor deposition, however, trades off with some of these limitations by forming high quality crystals, with larger throughput, at lower cost.

In this work, the synthesis of both ZnTe thin films and submicron structures via vapor deposition is presented as a function of Au catalyst. Poly-crystalline thin films were found to exhibit grain sizes up to 4.35 μm, which increased with increasing growth temperature due to reduced microstrain. Single-crystalline submicron features were found to exhibit suppressed O_2 defect related emission with growth temperature. The submicron structures were found to grow as long as 150 μm, facilitating the creation of embedded percolative networks for device fabrication.

2.3 Experimental Details

Growth of ZnTe thin films and submicron features were conducted in a horizontal single-zone quartz tube furnace via vapor deposition. Si (100) substrates were initially cleaned with isopropyl alchohol, acetone, and rinsed in deionized water. Prior to growth a subset of Si substrates were coated with a catalyst seed layer of sputtered 30 nm Au films. The growth furnace was then loaded with the Si substrates: a single trial with Au catalyst, and another trial without catalyst. After evacuating the furnace, the substrates were then "pre-baked" at 100 °C overnight to remove residual gas and moisture on the surface of the substrate and the inner wall of the tube furnace. Additionally, for trials with catalyst, the substrates formed islands of Au particles, facilitating wire growth. Before commencing growth at elevated furnace temperature, ZnTe powder (Alfa Aesar, 99.99%) was loaded into a ceramic boat as the source material. The ceramic boat was placed at the center of the tube furnace with highest temperature of 750 °C. This experimental setup of ZnTe growth is illustrated in Fig. 1, along with a summary of results from this work.

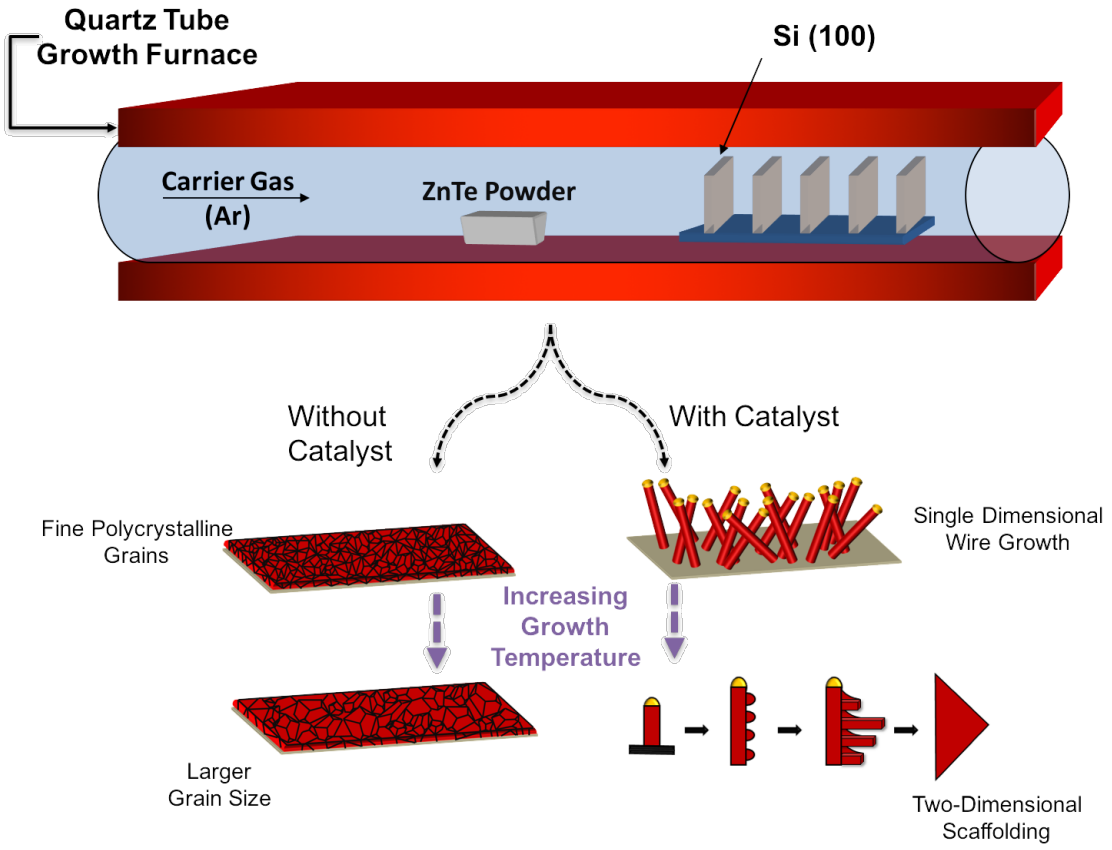

Figure 2.1: Experimental setup and summary of ZnTe growth

Argon was introduced as the carrier gas while the furnace temperature increased and a growth time of 1 hour was maintained. Gas flow was subsequently ceased as the furnace was cooled to room temperature. The characterization of the ZnTe thin films and nanostructures was performed using field emission scanning electron microscopy (FESEM), energy-dispersive X-ray spectroscopy (EDX), X-ray diffraction (XRD), High-resolution transmission electron microscopy (HR-TEM), photoluminescence (PL), and light scattering spectroscopy. Measurement of grain size distributions was conducted in imageJ software by tracing features from electron micrographs.

2.4 Results and Discussion

2.4.1 Poly-crystalline Thin Films

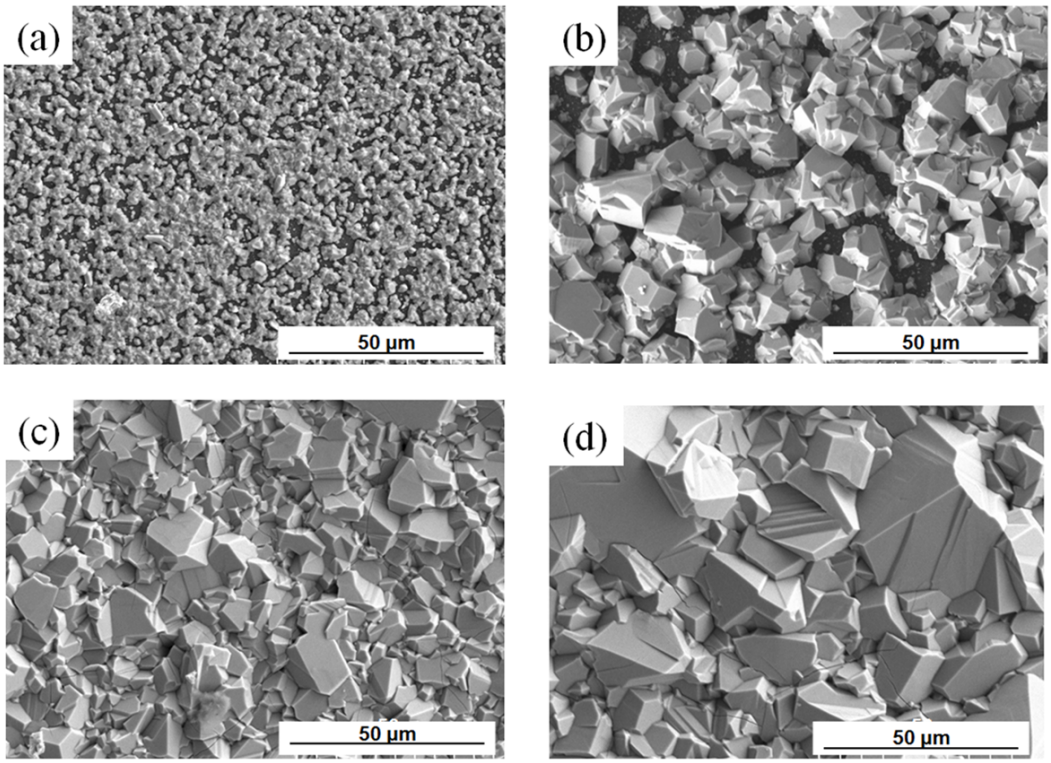

Figure 2.2: The SEM micrographs of the as-synthesized ZnTe thin films at growth temperatures of (a) 349 °C (b) 504 °C (c) 533 °C (d) 562 °C.

Fig. 2a, 2b, 2c and 2d show the SEM micrographs of the as-synthesized ZnTe thin films deposited on Si (100) substrate at substrate temperatures of 349 °C, 504 °C, 533 °C, and 562 °C , respectively, absent of a Au catalyst seeding layer. Nucleation, growth, and coalescence processes take place as temperature rises. Fig. 2a presents the nucleation of ZnTe small crystals in the early stages of film growth. As the growth temperature increases and crystallites grow (Fig. 2b-2d), the space between them decreases and poly-crystalline ZnTe films are formed through the coalescence of isolated ZnTe crystals on the Si surface. Furthermore, the increase in growth temperature also reduces the density of nucleation centers due to atoms on

the surface of the substrate having greater mobility. Substrate temperature is one of the key parameters in the vacuum deposition because it influences the crystallinity and composition of the deposited ZnTe thin films (Rao *et al.*, 2009).

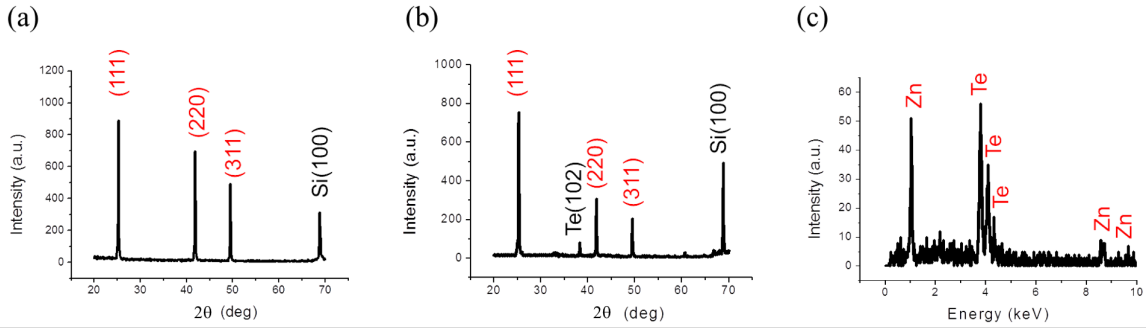

Figure 2.3: XRD pattern of the ZnTe layers on Si (100) substrates grown at (a) 533 °C and (b) 194 °C. (c) The EDX spectrum of ZnTe layers grown at 533 °C.

Fig. 3a shows the XRD pattern of the ZnTe thin films grown at 533 °C. The diffraction peaks at $2\theta = 25.26°$, 41.8°, 49.5°appear in the XRD pattern, which can be assigned to the (111), (220), and (311) planes of ZnTe repectively, and are consistent with reports of ZnTe thin films (Salem *et al.*, 2008; Shaban *et al.*, 2016; Mote *et al.*, 2012). Fig. 3a, 3b revealed that as-deposited films are poly-crystalline in nature and belonged to the zinc blende phase with a strong preferred orientation along the (111) direction. The crystallinity preference is largely a result of the silicon surface tending to reduce its surface energy, stemming from the lattice mismatch between the Si (100) substrate surface and the ZnTe crystal.

The XRD spectrum of ZnTe thin films shown in Fig. 3b reveal the presence of a small tellurium (102) peak at $2\theta = 38.15°$ for growth temperatures of 194 °C. This pattern indicates that as the substrate temperature is lower than 194 °C, there is not enough compensation for native tellurium interstitials to completely eliminate deviation from perfect stoichiometry. One possible origin for this deviation is due to the fractionation of zinc (Zn) and tellurium (Te) atoms during the evaporation

process. Te has a much lower vapor pressure compared to Zn at any given temperature (Khawaja *et al.*, 2005). The spectrum (Fig. 3c) of EDX confirm this trend with ZnTe thin films grown at 533 °C. Because the saturated vapor pressure of Zn is higher than that of Te, the ZnTe films will be Zn deficient. The average crystallite size (sometime referred to as sub-grain size), can be inferred through XRD by assessing Coherent Scattering Domains (CSD), i.e. regions of materials that scatter coherently (Opanasyuk *et al.*, 2012; Escobedo *et al.*, 2010). In the present study, XRD peak broadening analysis was used to estimate the crystallite sizes (D) and microstrain (e) by the Williamson-Hall (W-H) analysis. The method was based on the assumption that the crystallite size and strain line profiles are both presumed to exhibit a Cauchy dispersion relationship, and thus, crystallite sizes and microstrain can be modeled by the following relation (Shaban *et al.*, 2016; Mote *et al.*, 2012; Shaaban *et al.*, 2009):

$$\Delta(2\theta)cos(\theta_0) = \frac{\lambda}{D} + 4esin(\theta_0) \tag{2.1}$$

Where $\Delta(2\theta)$ is the full-width at half maximum (FWHM) of the diffraction peak, θ_0 is the diffraction angle, λ is the excitation wavelength of X-ray (1.5418 Å), D is the average crystallite size, and e is the microstrain. The FWHM of the zinc blende (111) peaks were calculated from recorded XRD data and decreases as the substrate temperature increases, as shown in Table 1. These results suggest that the crystallinity and preferential orientation increase with the increasing substrate temperature. The crystallite size increases with increasing substrate temperature, while the microstrain decreases. Shaaban et al. also reported this behavior and suggest that it may be due to the decrease in lattice defects among the crystallite boundaries with the crystallite size increasing (Shaaban *et al.*, 2009). The average crystallite sizes of ZnTe thin films grown on glass had been reported to be in the range of 25-80 nm (Salem *et al.*, 2008; Rao *et al.*, 2010; Balu *et al.*, 2010; Kumar

et al., 2014; Rathod *et al.*, 2011; Syed Basheer Ahamed *et al.*, 2010). However, ZnTe thin films grown on Si (100) single crystal substrates have much smaller FWHM, indicating larger crystallite sizes. In this work the average crystallite sizes was found to be up to 465 nm. The crystallite sizes, distribution of crystallite sizes, and surface morphology of poly-crystalline thin films are among the key factors that affect the performance of devices built on ZnTe thin films. Better performance may be expected from larger crystallite of poly-crystalline ZnTe thin films because of reduced carrier scattering from the boundaries.

Temperature	$\Delta\ 2\ \theta$			Crystal size (D, nm)	Microstrain (e)
	(111)	(220)	(311)		
194 °C	0.159	0.218	0.311	151.16	0.001688
533 °C	0.149	0.201	0.249	465.42	0.002565

Table 2.1: Extracted FWHM, crystallite size, and microstrain of ZnTe thin films grown at varying growth temperature.

In a poly-crystalline aggregate, the grain size and the crystallite size are seldom the same because the crystallite size is the size of the single crystal, whereas a grain may contain one or more than one crystallites. Traced SEM micrographs (Fig. 2) were analyzed in order to evaluate the average grain size of poly-crystalline thin films grown at different growth temperatures (Fig. 4). At higher growth temperatures, the average grain size of the ZnTe thin flims increased exponentially. The inset of Fig. 4 shows the Arrhenius plot of an average grain size of ZnTe thin film growth as a function of growth temperature, where E is the activation energy for boundary mobility or the migration energy. The average activation energy of the grain growth is calculated by regression analysis and a first order fit is found to be ≈0.26 eV (Fig. 4 inset). The activation energy E of different materials depend on the elementary

process of their atomic motion and generally it will be different for different elements and crystal structures. By using similar approach, Cho (Cho *et al.*, 2012), and Nieto (Nieto *et al.*, 2015) reported the activation energy of the grain growth for mesoporous TiO_2 structure and graphene nanoplatelet, respectively. Farkas et al. suggested a size-dependent grain boundary model by using molecular dynamics (Farkas *et al.*, 2007). In their model, grain growth occurs by the movement of grain boundaries and the mass transport is mainly determined by the grain boundary diffusion. Their model is similar to that proposed by Zhou et al. (Zhou *et al.*, 2005) in a study of size effects on grain boundary mobility in thin films. Their simulations of grain boundary migration in thin films show that the grain boundary mobility decreases with decreasing film thickness. The mobility decrease of thinner films is due to the boundary regions near the surface have a lower mobility. The simulation results provide clear evidence that grain boundary mobility is a function of the size of the system (Farkas *et al.*, 2007). The results of the inset of Fig. 4 imply a significant size effect, as the mobility of the boundaries increases as the grain size increases. The results can be explained by the model proposed by Zhou et al. that considers a size effect in the boundary mobility (Zhou *et al.*, 2005; Farkas *et al.*, 2007). As the growth temperature increase from 349 °C to 562 °C, an increased slope is observed, which implies there are fewer spaces between atoms at higher growth temperature, and therefore higher degree of crystallinity. The films deposited at higher substrate temperatures were found to have larger grains thereby enhancing optical and electrical properties of the ZnTe thin films.

2.4.2 Submicron Structures

Drastic morphological transitions occur when ZnTe is grown on substrates prepared with Au-coated catalyst seeds. Submicron features are illustrated in the SEM

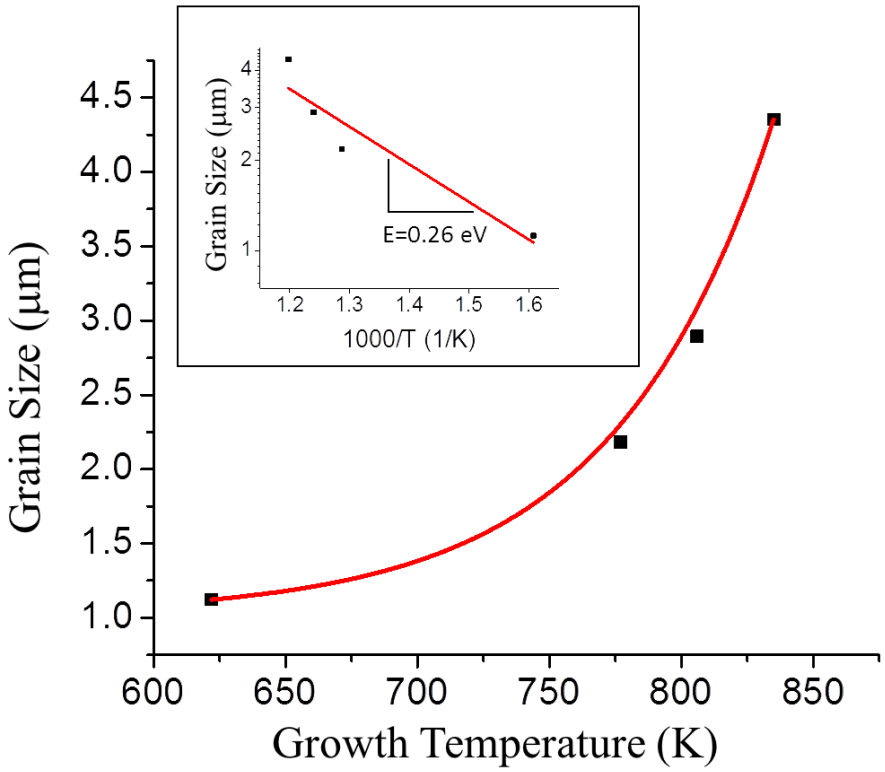

Figure 2.4: Average grain size as a function of growth temperature (inset: Arrhenius plot).

micrographs of Fig. 5a-d, where ZnTe wires were grown at temperatures of 504 °C, 511 °C , 526 °C, and 548 °C, respectively. Fig. 5e shows the SEM micrographs of vertical ZnTe wires grown on Si (111) substrate at 526 °C, which support vertical device fabrication. The predominant mechanism that drives ZnTe nanostructural formation is that of the vapor-liquid-solid (VLS) growth phenomenon (Li *et al.*, 2011a; Devami *et al.*, 2011a). Several hundreds of micron to millimeter long ZnTe wires protruding from edge of the silicon substrates are shown in the inset of Fig. 5d. The SEM micrographs clearly indicate that the top of ZnTe wires still contain an unreacted gold catalyst, indicating VLS mechanisms in effect. Several other reports have confirmed growth of ZnTe wires that range from 10-150 μm (Liu *et al.*, 2013b; Li *et al.*, 2011a; Davami *et al.*, 2012; Cao *et al.*, 2011a) and the lengths of ZnTe wires grown at 548

°C, from this experiment extend even longer than 150 μm. Between 504-548 °C, the increase of temperature causes longer diffusion distance of the Zn and Te atoms along wire surface and increases the equilibrium concentration of adatoms. This effect increases the diffusion flux to the base of wires, and consequently to the top of wires thereby increasing the length of the wires.

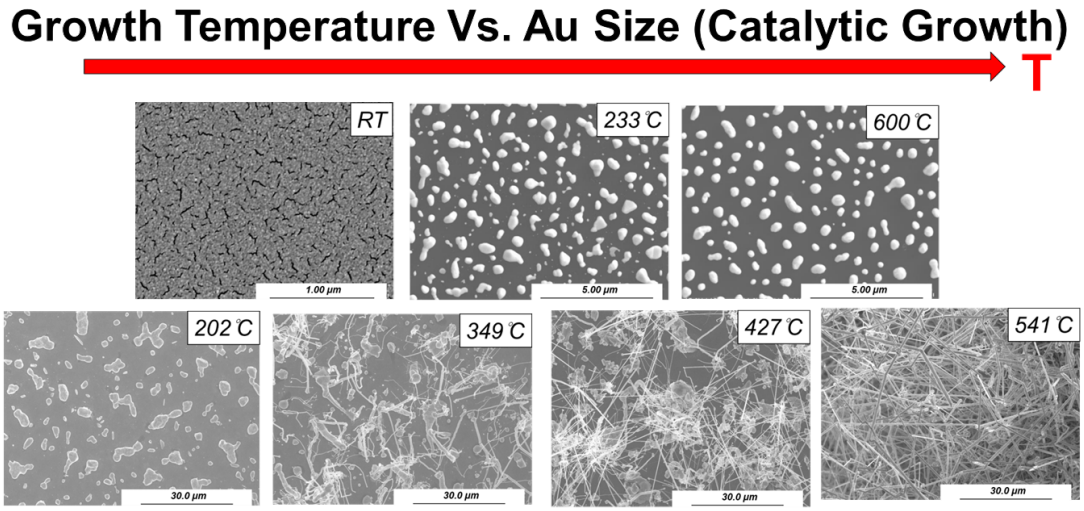

Figure 2.5: Morphological Variation of nanostructures as a function of growth temperature and Au size

As seen in Figure 2.5, the wire diameters also have a strong dependence on the substrate temperature, and can be attributed to two predominate mechanisms. First, higher substrate temperatures will increase the size of catalyst islands before growth due to coalescence. During the VLS growth process, the melting point of nanoclusters as catalysts decreases with the decreasing size in the nanometer region; therefore, catalysts with larger diameter will tend to condense in the higher temperature zone (Devami *et al.*, 2011a). Secondly, the contact angle between the wires and catalyst droplet decreases at higher temperature, thus leading to increased wire thickness (Devami *et al.*, 2011a). In this work, when the growth temperature rises from 504Âř °C to 548 °C, the diameter of ZnTe wires increases from 90 nm to 230 nm.

From the HR-TEM image (Fig. 6) of a single ZnTe nanowire, an identical periodic

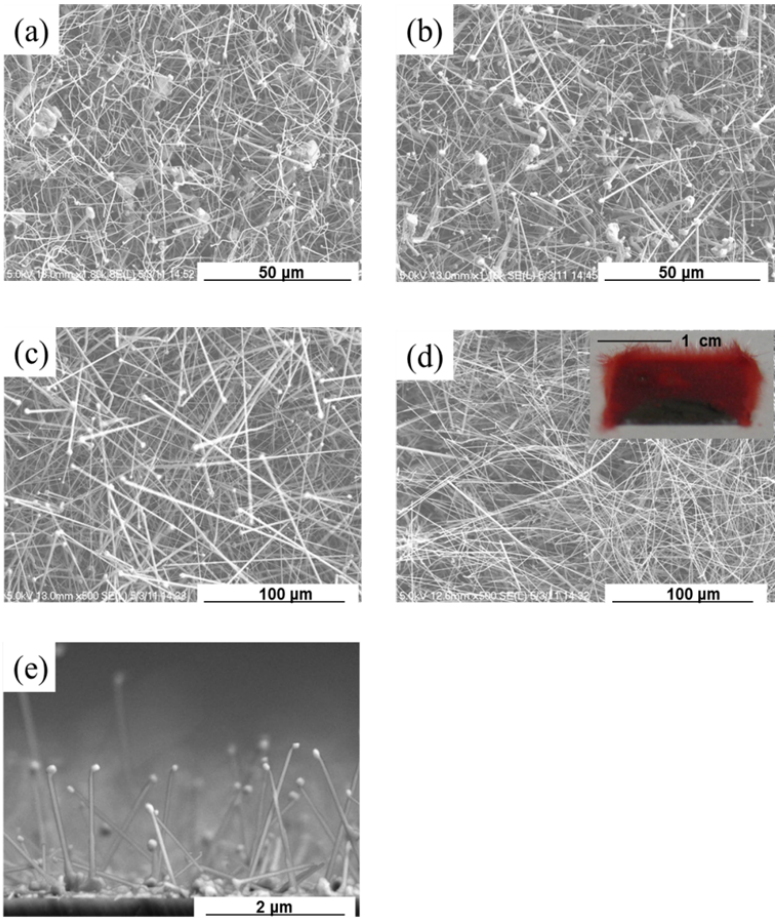

Figure 2.6: SEM micrographs of the ZnTe wires that were grown on Si (100) at temperatures of (a) 504 °C, (b) 511 °C, (c) 526 °C, and (d) 548 °C with optical image of grown wires (inset). (e) Cross sectional micrograph of the ZnTe wires, grown on Si (111) at 526 °C.

orientation is found along the length of the wire, revealing its single crystallinity and uniformity. The HR-TEM image also shows the nanowire having planes with a lattice spacing of 3.5 $\AA$, corresponding to the spacing of the (111) plane of the ZnTe cubic structure. ZnTe crystals grow via close-packed planes {111} and this has also been observed by others (Li *et al.*, 2011a; Cao *et al.*, 2011a; Meng *et al.*, 2008a). Synthesis of materials in nano-scale are driven by the tendency of surfaces to reduce their surface energy. Li et al. has discussed the lower-energy (111) planes of ZnTe nanostructures (Li *et al.*, 2011a), indicating that the crystal preferentially grows via close-packed

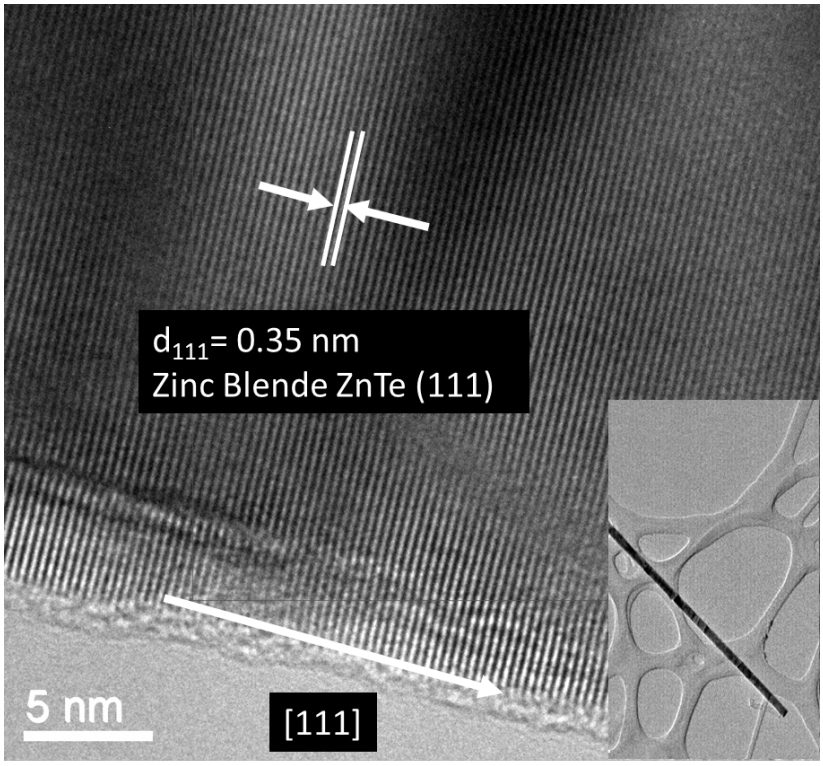

Figure 2.7: HR-TEM of single ZnTe wire.

planes {111} to minimize the surface energy. Because surface energy has an impact on the liquid dynamics and nucleation, ZnTe nanowires form along the {111} plane to minimize the surface energy, and align its {111} facets upward in the initial stage. Photoluminescence spectroscopy was also used to characterize the optical property of the synthesized ZnTe nanostructures. Reports of strong band edge emission in PL from ZnTe films deposited by pulsed laser deposition techniques has been notably difficult to obtain at room temperature (Ghosh *et al.*, 2012; Xu *et al.*, 2016). It has often been attributed to the increase of zinc vacancy (V_{Zn}) density and deviations from stoichiometry (Ghosh *et al.*, 2012; Xu *et al.*, 2016). With the growth techniques employed in this work, ZnTe nanowires have shown clear band edge emission at room temperature (Fig. 7). A strong green emission peak centered at about 550 nm is observed in the PL spectra of Fig. 7. As shown in Fig. 7, a series of PL spectra of

ZnTe wires grown at 504 °C, 511 °C, 519 °C, 526 °C, 533 °C, 541 °C, 548 °C, 555 °C, 562 °C, 570 °C, and 577 °C is demonstrated. The PL peak centered at 550 nm (2.26 eV) is due to the band-edge transition. The low-energy portion of the PL data corresponding to peaks energies below 2.26 eV have been attributed to the effects of oxygen incorporation and its phonon replicas (Ye *et al.*, 2014). The broad PL band centered at 725 nm (1.71 eV) is attributed to emission from an exciton bound to isoelectronic oxygen substituting Te atoms (O_{Te}) (Kang *et al.*, 2006a; Zhou *et al.*, 2014). It was reported that the red emission in the PL spectrum of ZnTe was found at the wavelength range of 660-810 nm (Pak *et al.*, 2012; Wang *et al.*, 2009).

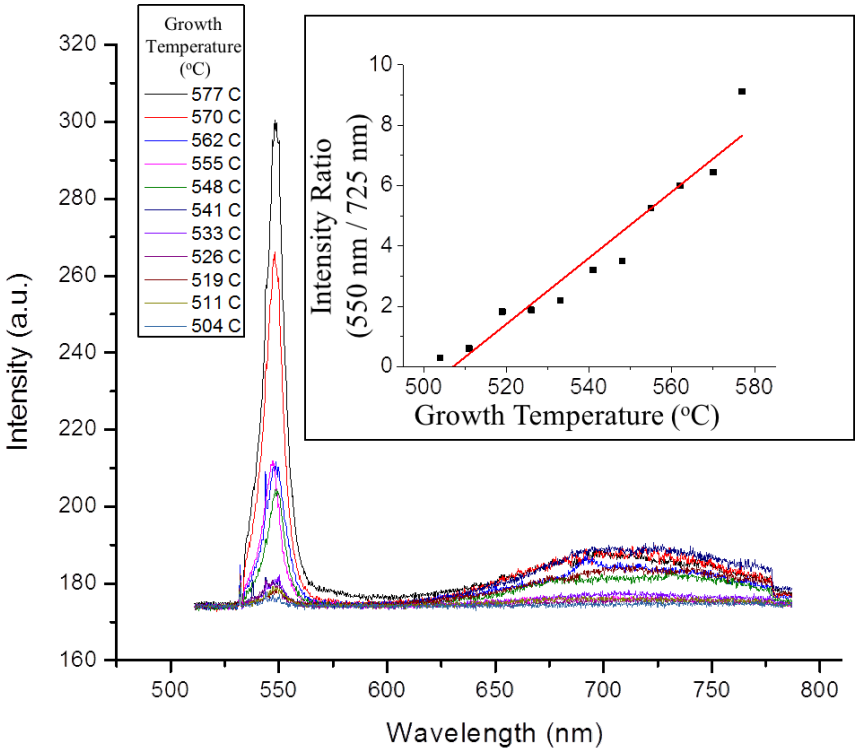

Figure 2.8: Room-temperature PL spectra of ZnTe wires grown at varying temperature, (inset: ratio of relative intensity of band edge peak (550 nm) to oxygen defect related peak (725 nm) as a function of temperature).

Although the band edge peak intensities vary with different growth temperature, the variation from different growth temperature is only approximately 1-3 nm, and these peak energies agree with reported values of bulk-ZnTe (Garcia *et al.*, 2001).

The 550 nm peak intensity increased with increasing growth temperature, indicating higher crystal quality with less impurities and defects. In relation to ZnTe growth, higher growth temperature may reduce the oxygen content during and after deposition.

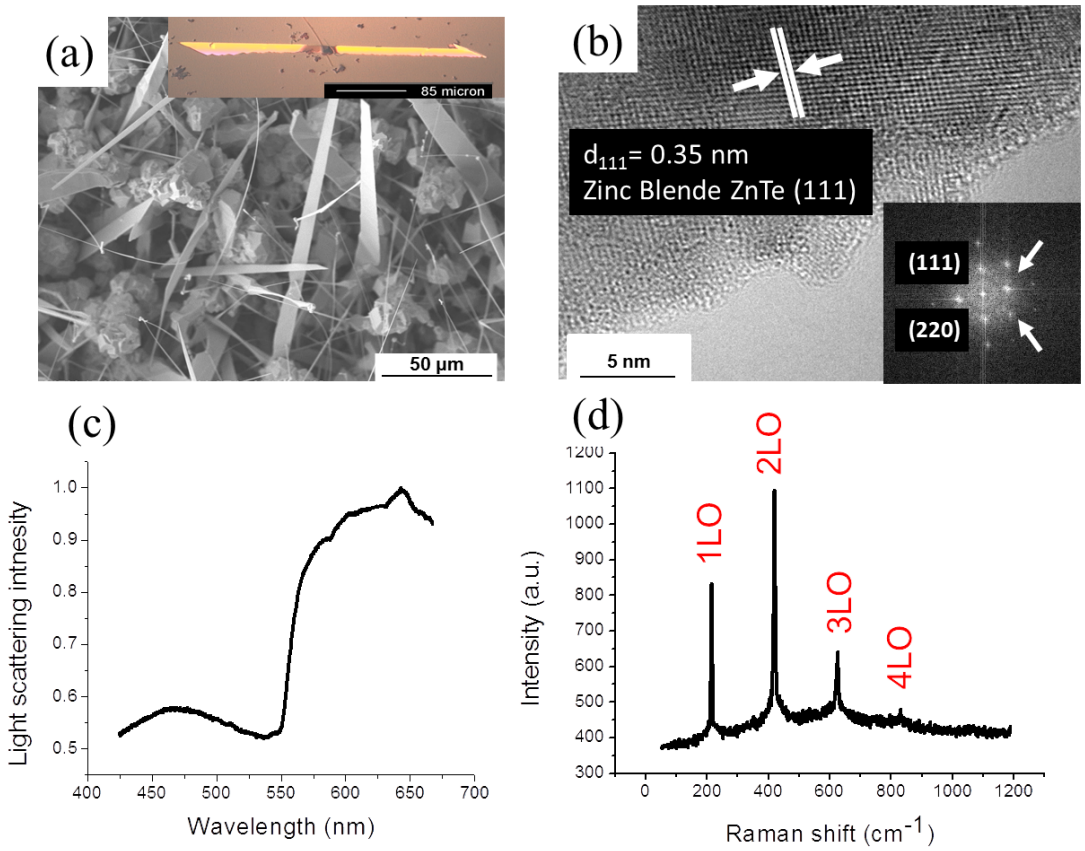

Figure 2.9: (a) The SEM micrograph of ZnTe sample grown at a 570 °C (inset: optical image of ZnTe sheets). (b) HR-TEM of a single ZnTe submicron sheet. (c) Light scattered spectrum of ZnTe sheets. (d) Raman spectrum of ZnTe sheets.

The inset of Fig. 7 illustrates the increasing ratios of the PL peak intensities at the band edge of ZnTe (550 nm) to that of O_2 related defects (725 nm) peak, for increasing growth temperature increase. As previously discussed, when growth temperature decreases oxygen defects form along the ZnTe wires. Nam et al. reported similar observations, in which ZnTe epilayers grown on thermally preheated at 430-630 °C GaAs substrates by hot wall epitaxy (HWE) (Nam *et al.*, 2000). The thermal

preheating temperature dependence of the ratios of the intensities of oxygen-bound exciton peak to band-edge exciton peak was examined, and they found that with increasing preheating temperature, the intensities of the oxygen-bound exciton peak related to an oxide layer on the GaAs surface generally decreased, suggesting that thermal preheating of substrates play an important role in determining the crystal quality of epilayer. Moreover, Kang et al. suggest that even small amounts of oxygen in ZnTe may exacerbate the low-energy portion of the PL spectra (Kang *et al.*, 2006b). The presence of oxygen is most likely due to oxygen or water residue in reaction chamber. The peak intensity ratio increases with the growth temperature, indicating that higher growth temperature can prevent the unintended oxygen related defects.

A variety of other submicron ZnTe features, apart from wires, were also observed. Fig. 8a shows optical and SEM micrographs of large ZnTe micro-sheets of about 150-200 μm in length grown at a 570 °C, in addition to a heterogeneous mixture of other nano structures. Once again, the growth temperature has a strong influence on the morphology of the ZnTe and in this temperature regime, a range of structures including nanowires, sheets, springs can emerge. The growth morphologies are sensitive to the substrate temperature, and consequently higher temperatures usually lead to the growth of ZnTe sheets with micron-scale sizes. Previous reports of sheets grown by vapor transport attribute the morphology to high substrate temperature and high source temperature (Devami *et al.*, 2011a; Fasoli *et al.*, 2006). Source temperature regulates the amount of source material impinging on the sample and higher source temperature increases the amount of source material delivery (Fasoli *et al.*, 2006). On the other hand, substrate temperature determines the sample surface kinetics and higher substrate temperature enhances the surface mobility of the adsorbed atoms, allowing side growth and forming the sheets. When surface mobility is high enough to ensure proper migration and incorporation for adsorbed atoms, epitaxial growth

occurs and leads to a sheet morphology. As reported, Park et al. demonstrated ultrawide ZnO nanosheets with their formation mechanism (Park *et al.*, 2004b), and suggested the possible growth mechanism of the sheet structure by a "1D branching and 2D filling" process. As the substrate temperature and the oxygen content increases, the nanostructures evolve from nanowires (1D) to combs (2D), concluding with sheets (2D) through planar fill-up mechanism. Importantly, this fill-up process occurrs under higher supersaturation state of reactant vapors (Park *et al.*, 2004b), and sheet formation occurs with additional epitaxy on axially growing wires at higher temperatures. Fig. 8b shows the HR-TEM image of a small piece of ZnTe sheets. The growth direction of the sheet is along the [111] direction and the TEM confirms the single crystalline nature of the ZnTe sheets. The inset of Fig. 8b shows the diffraction pattern of the sheet and the result is consistant with other report (Yim *et al.*, 2009). A few nanometer thick amorphous shell is also visible on the sheet walls.

Light scattering measurements of ZnTe sheets is shown in Fig. 8c, which is used to characterize material surfaces. Strong light absorption near the energy band gap of ZnTe (550 nm) indicate high optical quality of ZnTe sheets. A Raman spectrum at room temperature of single ZnTe sheet grown at 570 °C is shown in Fig. 8d. ZnTe has a cubic crystal structure of the zinc blende type with two atoms per unit cell. The first order Raman spectrum consists of two lines. The highest in frequency is denoted the longitudinal optical (LO) branch and the lowest is the doubly degenerate transverse optical (TO) branch. In Fig. 8d, the Raman shift indicates the 1LO(Γ), 2LO(Γ), 3LO(Γ) and 4LO(Γ) modes, found at 214 cm^{-1}, 420 cm^{-1}, 625 cm^{-1}, 830 cm^{-1}, respectively. The frequency of the modes correspond to the values typical of high-quality ZnTe single crystals and indicate high optical structural quality of the sheets. It has also been demonstrated that under a resonant excitation on the exciton, several ZnTe LO mode replicas can be observed in good quality crystals

(Utama *et al.*, 2013a; Zhang *et al.*, 2012). In short, the ZnTe sheets in this work are single-crystalline, and ranged in size from 50-200 μm in length and 1-10 μm in width, which may facilitate further transistor applications (Zhang *et al.*, 2008b).

2.5 Conclusion

In summary, poly-crystalline ZnTe thin films and submicron single-crystalline features have successfully been synthesized via vapor deposition technique. The different morphologies were controlled through either the absence or the presence of gold (Au) catalyst deposited as a seeding layer on silicon (100) substrates before growth. These results indicate that the ZnTe thin films exhibited poly-crystalline structure, and the grains imply a significant size effect, as the mobility of the boundaries increases as the grain size increases. Submicron wires and sheets exhibited single-crystal structures and the preference for the (111) orientation indicates that the crystal preferentially grows via close-packed planes {111} to minimize the surface energy and the peak intensity ratio (550 nm/725 nm) of PL increases with the growth temperature indicated that the growth temperature plays an important role in the crystal quality. The high quality single crystal submicron features, which extend up to several microns in length can facilitate device applications through percolating networks. The vapor deposition approach with the use of Au catalyst, can synthesize ZnTe thin films and submicron structures at low cost.

Chapter 3

SYNTHESIS AND FABRICATION OF ZNTE NANOSHEET FIELD EFFECT TRANSISTORS AND PHOTODETECTORS

3.1 Abstract

In this work, we report the fabrication of ZnTe nanosheet devices grown by a high temperature growth process followed by low temperature fabrication process. Single crystal ZnTe nanosheets were grown on Si by heating ZnTe powder in a tube furnace, promoting the synthesis of high quality of ZnTe nanosheets. Scanning electron microscopy, atomic force microscopy, and transmission electron microscopy indicate ordered and single crystalline sheets have been obtained. Transistor devices were then fabricated with the nanostructures. The current-voltage characteristics were used to study the transport behavior of single ZnTe nanowires and nanosheets. Predominant p-type behavior was observed, an on/off ratio of 3.7×10^3 was found, and a field effect mobility of 4.11 cm^2/V-s. The photoconductivity of these nanosheets was also investigated under the illumination of a green diode laser with varying intensity. A responsivity of 2.62×10^5 A/W and a photoconductive gain of 6.10×10^5 was determined for nanowires, as well as 110.59 A/W and a photoconductive gain of 257.76 for nanosheets. These values are quite comparable to similar ZnTe nanodetector devices. The mechanism for photoconductive gain in ZnTe has largely been attributed to surface states creating trap recombination centers leading to longer carrier lifetimes. These results reveal that single ZnTe nanowires are excellent candidates for applications for nanoscale photoconductive detectors.

3.2 Introduction

Single and two dimensional nanostructures have garnered much interest in regards to their realization toward functional devices (Lieber and Wang, 2007; Agarwal and Lieber, 2006; Wang, 2009). Two-dimensional nanostructures possesses very unique advantages by nature of their geometry, including mesoscopic assembly, planar surfaces, and the ability to be utilized as miniature substrates (Park *et al.*, 2004c; Zhang *et al.*, 2011). Synthesis techniques of such nanostructures, including nanowires and nanosheets, have been widely studied, and these structures have been utilized for a variety of applications including sensors (Ramgir *et al.*, 2010; Belagodu *et al.*, 2012; Cui *et al.*, 2001), field effect transistors (Xu *et al.*, 2012; Cui *et al.*, 2003), photovoltaics (Tian *et al.*, 2009, 2007), and photodetectors (Yu *et al.*, 2012; Young and Liu, 2015; Soci *et al.*, 2007b). Certain interest has been placed on Zinc Telluride, a II-VI compound semiconductor, with a band gap of 2.26 eV and exhibits preferential p-type doping (Ruda, 1991; Larach *et al.*, 1957). Doped and undoped ZnTe films have traditionally been used to realize a variety of optoelectronic devices such as photodetectors (Chang *et al.*, 2001) and intermediate solar cell layers (Gessert *et al.*, 2009; Rioux *et al.*, 1993; Spath *et al.*, 2005b). Additionally, ZnTe has often been compared to GaAs and ZnS systems in regards to its superior electro-optical coefficient and electron-LO-phonon (polaron) coupling constant (Kumagai and Kobayashi, 2012; Pelekanos *et al.*, 1991; Kaminow and Turner, 1966; Xue and Zhang, 1997), as well as GaN/InGaN emitters for circumventing the problem of phase segregation in compositional band edge engineering (Osamura *et al.*, 1975; Moon *et al.*, 2001). Most recently, the growth mechanisms describing the formation of various ZnTe nanostructures have been heavily explored (Devami *et al.*, 2011b; Li *et al.*, 2005; Janik *et al.*, 2007; Meng *et al.*, 2008b; Guo *et al.*, 2008; Yong *et al.*, 2007; You-Wen *et al.*, 2007).

Additionally the use of ZnTe nanowires has led to the successful fabrication of field effect transistors (Cao *et al.*, 2012; Huo *et al.*, 2006a; Li *et al.*, 2010a, 2011b; Liu *et al.*, 2013a; Wu *et al.*, 2012) and photodetectors (Zhang *et al.*, 2008a; Liu *et al.*, 2013a; Li *et al.*, 2011b). However, the this discussion and an adequate comparison have been scarce among ZnTe structures exhibiting a unique, 2D nanosheet configuration. In this study, ZnTe nanowires and nanosheets have been synthesized and characterized. Their relative performance in terms of electrical conductivity, transfer behavior, and photoresponse have been compared. It has been found that the pronounced effect of surface trap states render unfavorable transfer behavior for nanowires, but contribute to the greater photodetection sensitivity, relative to nanosheets.

3.3 Experimental Details

Zinc Telluride (ZnTe) nanosheets and nanowires were synthesized in a quartz tube placed in a single zone horizontal tube furnace. Si substrates [100] were cleaned successively with acetone, isopropanol, and deionized water. Nanostructure synthesis was facilitated by a VLS growth technique (Huo *et al.*, 2006b; Meng *et al.*, 2008b; Devami *et al.*, 2011b). ZnTe (99.99%) powder was placed at the center of the quartz tube and Au-coated (30 nm sputtered) silicon substrates were placed at downstream from the source material.

After the quartz tube was evacuated, the samples were then held at 100 °C overnight before commencing synthesis. High purity argon was introduced at a rate of 140 sccm (standard cubic centimeters per minute) into the quartz tube. The powder was elevated to a temperature of 750 °C and the temperature of the substrates were maintained at approximately 570 °C for the nanosheets and at 475-530 °C for the nanowires. A pressure of 20 torr was maintained within the tube furnace throughout the entirety of synthesis. After a growth time of 5 hours, the furnace was allowed to

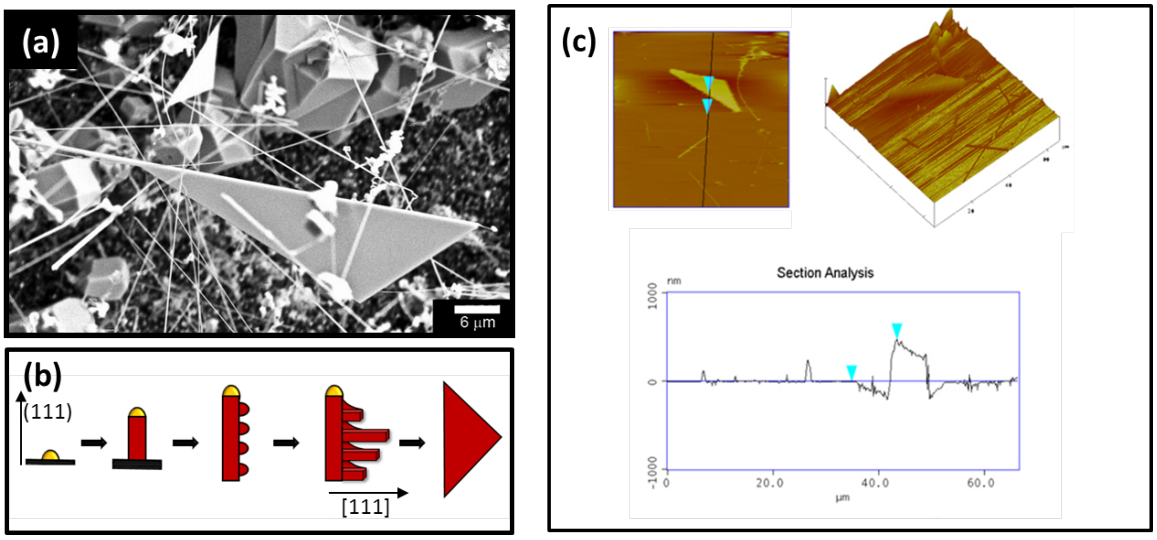

Figure 3.1: (a) SEM micrograph of synthesized ZnTe nanostructures. Nanosheets are observed with the presence of a single nanowire protruding and establishing the foundation of the nanosheet base. (b) Illustration of growth and filling process forming ZnTe nanosheets (c) AFM and profile analysis of single ZnTe nanosheet

cool naturally to room temperature, while maintaining the above mentioned flow rate and pressure conditions. Based on the above growth parameters, both nanosheets and nanowires were formed. The samples were further characterized with a field emission scanning electron microscope (SEM, Hitatchi S4700-II), operated at 15 kV, a atomic force microscope (Digital Instruments) for profile analysis, and a transmission electron microscope (TEM, JEOL JEM 2010F) attached with an energy-dispersive X-ray spectrometer (EDAX).

Assembly of single ZnTe nanosheet and nanowire-based devices was accomplished with a standard microelectronic-fabrication process. Transfer characteristics of the FET and the current-voltage (I-V) characteristics of the photodetectors were measured using a probe station connected to a Keithley 4200 Semiconductor Characterization System (SCS). Devices were then illuminated under a 532 nm, power modulated, green diode laser. All electrical measurements were collected at room temperature in air.

3.4 Results and Discussion

Figure 3.1(a) shows the scanning electron micrograph (SEM) of various high quality single crystal ZnTe nanostructures as confirmed by previous XRD analysis. The ZnTe nanostructures are found to be in different stages of growth, in addition to dispersed Te precipitates (confirmed with EDX). Measurements from the microcraph reveal that nanowire length ranges from tens to hundreds of microns that their diameters range from 90-230 nm. Very distinct triangular growth structures, nanosheets, have also been found throughout the synthesis. AFM (Figure 3.1(c)) analysis confirms the thickness of the ZnTe nanosheets to be on the order of 100-500 nm. Evidence of nanowire artifacts are seen throughout each ZnTe nanosheet, as they seem to be present along the base of each nanosheet formation.

Figure 3.1(b) illustrates the proposed growth formation of ZnTe nanosheets. As discussed in reports of ZnO nanosheet growth (Park *et al.*, 2004a, 2005), gold cat-

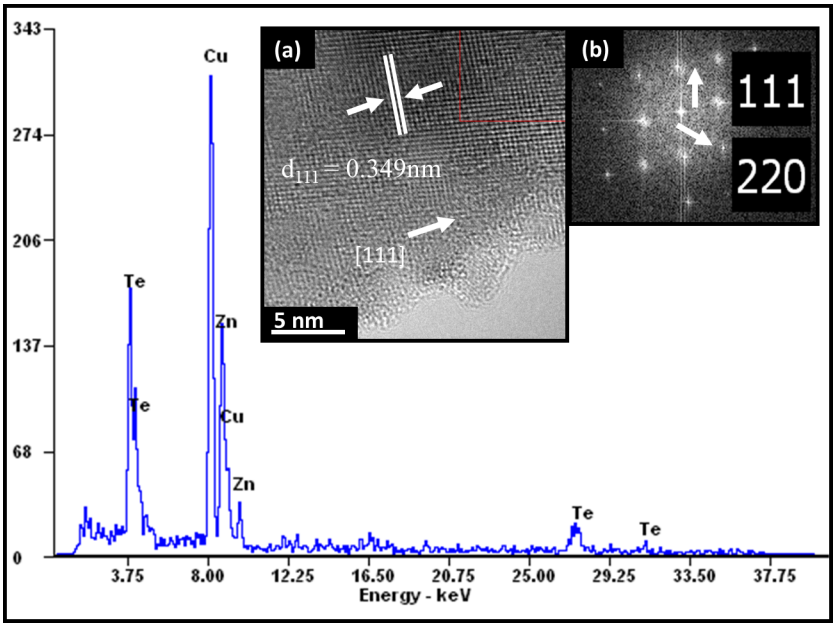

Figure 3.2: EDX Spectrum of ZnTe nanosheet (a) HRTEM Micrograph of ZnTe nanosheet illustrating the (111) plane spacing of 0.349 nm with (b) corresponding SAED Pattern

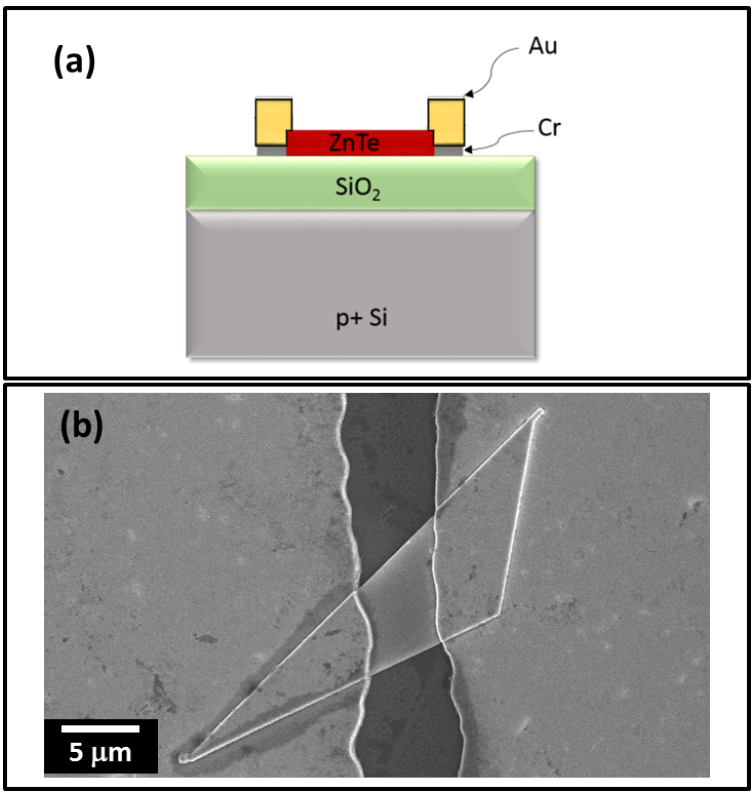

Figure 3.3: (a) Schematic of ZnTe nanostructure devices and (b) SEM micrograph of single nanosheet device

alyzed VLS growth has been shown in several cases to lead to secondary dendritic side branched growth. In the final stages of formation, the dendrites will tend to fill the interspaces monolithically. This growth is proposed to occur on the Te-terminated surface in the <111> family of directions because this face has the lowest surface energy, and higher growth rate than the Zn-terminated surface. The low energy surfaces grow to decrease the overall surface energy of the crystal.

Previous studies of ZnTe nanostructures growth offer multiple explanations in regards to planar nanostrucutred ZnTe formation, but not specifically large-scale nanosheets as described above. One common thread, however is that high temperature and high vapor pressure lead to a more diffusion-limited growth, which promotes secondary formation. Utama et. al proposes that nanobelts are formed from 2D growth at high temperatures from VS in the lateral direction in addition to axial

growth from VLS. This 2D growth has a pronounced tapering associated with the structure. In regards to the twinned nanobelts, it has also been found that the Te-terminated facet is more chemically and catalytically active than Zn, making it an active facet for lateral crystal growth (Utama *et al.*, 2013b). Devami et. al also note that the high temperature ribbon/belt formation is from the 2D epitaxy concurrent with axially growing wires. A combination of increased flow rate, and higher temperatures combined with rate-limited precursor, the nanowires formed are short and thin in nature while other structures form such as multiple prongs on wire tips. With an increase in temperature these multi-pronged wires taper and with an increase in temperature and nanoribbons begin to form (Devami *et al.*, 2011b).

Figure 3.2(a) shows the high resolution TEM (HRTEM) micrograph of a ZnTe nanosheet, which confirm a single-crystalline lattice structure. The ZnTe spacings were extracted by a fast fourier transform (FFT) analysis. The zinc-blende ZnTe structure with a lattice spacing of 0.349 nm which corresponds to the d-spacing of the (111) plane of the ZnTe structure. Additionally, the lattice spacing of d=0.3 nm corresponds to the (200) plane of the zinc blende ZnTe structure. An SAED pattern is also shown in Figure 3.2(b) which indexes the [111] and [220] directions. An EDX spectrum is also found in Figure 3.2 which confirms the nanosheet composition of Zn and Te. The presence of the Cu signal arises from the Cu TEM grid.

Both nanostructures were then fabricated into transistor devices through a conventional photolithographic patterning process on a heavily doped p+ Si substrate, with a 200 nm thermally grown SiO_2 back-gated insulator. A layer of Cr/Au (10 nm / 250 nm) was thermally evaporated, forming top contacts. The schematic of this device structure is seen in the inset of Figure 3.3(a). The fabricated devices were formed with 5 μm channel lengths extended between electrodes. An optical micrograph of both device types can be found in the SEM of the nanosheet device found

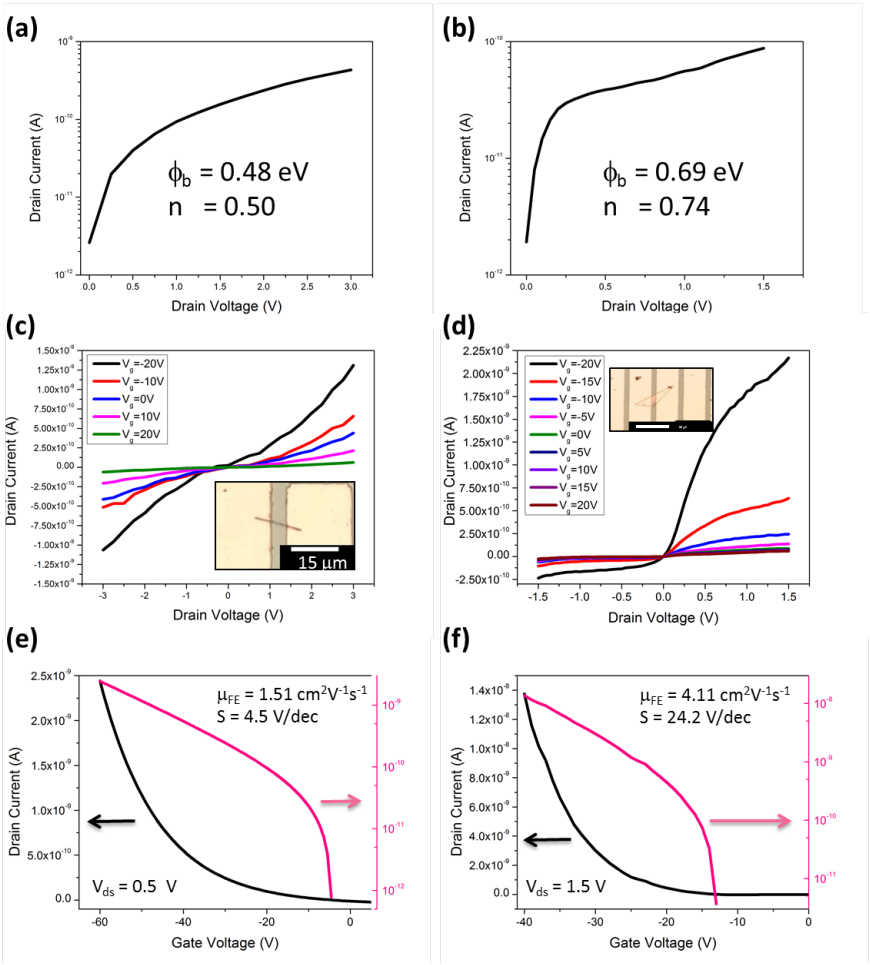

Figure 3.4: Electrical characteristics of nanowire (first column) and nanosheet devices (second column). (a) and (b) I-V curves of nanowire and nanosheet devices under zero gate-bias and no illumination for contact barrier analysis. (c) and (d) I_{ds} vs. V_{ds} curves of nanowire and nanosheet devices at varied V_{gs}. Note: Reduced conductivity as V_{gs} increases indicating p-type behavior (inset shows optical micrograph of both devices) (e) and (f) I_{ds} vs. V_{gs} curves for nanowire and nanosheet devices, respectively.

in Figure 3.3(b).

The current-voltage (I-V) response of both ZnTe nanowire and nanosheet devices with no gate bias and in dark conditions is found in Figure 3.4 (a) and (b). Both devices displayed slight nonlinearity and asymmetry based on the polarity of the applied voltage. This indicates the presence of a contact barrier between Cr/Au and ZnTe, and fitting the 0 gate-bias plot to a thermionic emission model, we are able

to extract the Schottky barrier height (ϕ_B) and ideality factor (n) according to the following relationships (Sze and Ng, 2006):

$\phi_B = \frac{kT}{q} ln(\frac{A^* T^2}{J_o})$

n = $\frac{q}{kT} \frac{dV}{d(ln(J))}$

where k is the boltzmann constant, T is the absolute temperature (taken at room temperature), A^* is the effective Richardson constant (taken to be 72 $\frac{A}{cm^2 K^2}$) (Bhunia and Bose, 2000), J_o is the extrapolated current density intercept, q is the elementary electronic charge and dV/d(ln(J)) is the inverse of the slope of the semi-logrithmic I-V plot. In this case, a barrier height of 0.48 eV with an ideality factor of 0.50 was determined for nanowires and 0.69 eV with an ideality factor of 0.74 nanosheets. Little has been reported specifically of Schottky barriers on ZnTe nanostructures formed with Cr/Au. However reports of Schottky barriers formed with Au on bulk ZnTe(**?**) have demonstrated barrier heights of 0.69, and 0.44 eV with Ti/Au on ZnTe quantum dots (Zielony *et al.*, 2012), while others have reported ohmic behavior(Meng *et al.*, 2009). In this work, the increased conductivity of the nanowire, due to surface dominated transport and self-compensation), gives way to an increased current density and increased inverse-slope (due to increased SRH recombination), thereby reducing the Schottky barrier height and ideality factor, as compared to the planar sheet configuration.

A family of I_{ds} vs. V_{ds} curves at various gate voltages is also shown for a single nanowire (Figure 3.4(c)) and a single nanosheet (Figure 3.4(d)). Decreased conduction with increasing back-gate voltage (ranging from -15 V to 15 V in step sizes of 5 V), was exhibited for both cases. This decrease in drain-source current against increasing gate bias is expected and indicative of p-type behavior (Zhang *et al.*, 2008a; Li *et al.*, 2011a; Liu *et al.*, 2013a). P-type conductivity has often been attributed to Zn vacancies intrinsically present in the ZnTe lattice. These self-compensation

Device Structure	$g_m(nS)$	μ_{FE} cm^2/V-s	I_{on}/I_{off}	S (mV/dec)
ZnTe Bulk (Fujita *et al.*, 1975)	n.a.	31 (hall)	n.a.	n.a.
ZnTe NW (Liu *et al.*, 2013a)	488.5	11.3	3.3×10^3	n.a.
ZnTe NW (Cao *et al.*, 2012)	n.a.	1.76×10^{-4}	5	n.a.
ZnTe NW (twinned) (Li *et al.*, 2011a)	0.34	0.11	1.3	n.a.
ZnTe:Cu NW (Huo *et al.*, 2006a)	1.7	1	n.a.	n.a.
ZnTe:Ph (.5 at %) NW (Cao *et al.*, 2012)	n.a.	4.47×10^{-3}	n.a.	n.a.
ZnTe:Sb nanoribbons (Wu *et al.*, 2012)	8.1	0.94	1.6	2.94×10^5
ZnTe: nanoribbons (Li *et al.*, 2010a)	0.4	0.01	n.a.	n.a.
ZnTe:N: nanoribbons (Li *et al.*, 2010a)	78.4	1.2	n.a.	n.a.
ZnTe NW (this work)	1.5	1.51	3.16×10^3	4.47×10^3
ZnTe nanosheet (this work)	212.7	4.11	3.75×10^3	2.42×10^4

Table 3.1: Comparison of ZnTe nanostructure-based transistor performance metrics

effects have been elaborated on extensively in the discussion of II-VI materials, and are generally ascribed to variations in dissociation pressure for the comprising species that form the final semiconductor crystal, thereby leading to deviation from perfect stoichiometry (Marfaing, 1996). In this instance, Zn has a higher vapor pressure than Te, thereby leading to a higher Te content in ZnTe nanostructures, as well as leading to the formation of Te crystillite precipitates, both of which have been present in the growth (Figure 4.4(a))). The defect chemistry and the underlying reaction can be expressed as:

$$V_{Zn}{}^{x} \rightleftharpoons V_{Zn}{}^{'} + h^{0}$$

$$V_{Zn}{}^{'} \rightleftharpoons V_{Zn}{}^{''} + h^{0}$$

$$V_{Zn}{}^{x} \rightleftharpoons V_{Zn}{}^{''} + 2h^{0}$$

In order to preserve charge neutrality, the excess Te forces Zn^{2+} into a meta-stable trivalent state with a weakly-bound hole. In the context of the ZnTe band structure, the combination of neutral and ionized Zn vacancies form sets of shallow acceptor levels within the ZnTe bandgap.

The transfer characteristics (I_{ds} vs. V_{gs}) of both FETs are also plotted linearly and logarithmically in Figure 3.4(e) and (f). For nanowires, gate voltages were swept from -40 to 10 V at a drain voltage (V_{ds}) of 1.5 V. Likewise, for nanosheets, gate voltages were swept from -55 to -35 V at the same drain-source bias. From this analysis, it is found that the on/off ratio of 3.2×10^3 for nanowires and 3.7×10^3 for nanosheets. The threshold voltage (V_{th}) was estimated by extrapolating the intersection of the tangent line in the linear region to the V_{gs} axis. This was estimated to be -8 V for nanowire and -22.75 V nanosheet devices.

The hole field-effect mobility for both device structures was calculated using the relationship $\mu_{FE} = g_m L^2/(V_{ds} C_g)$, where gm is the transconductance measured in the linear region of the transfer curve (g_m=$d(I_{ds})/d(V_g)$, L_g is the channel length (5

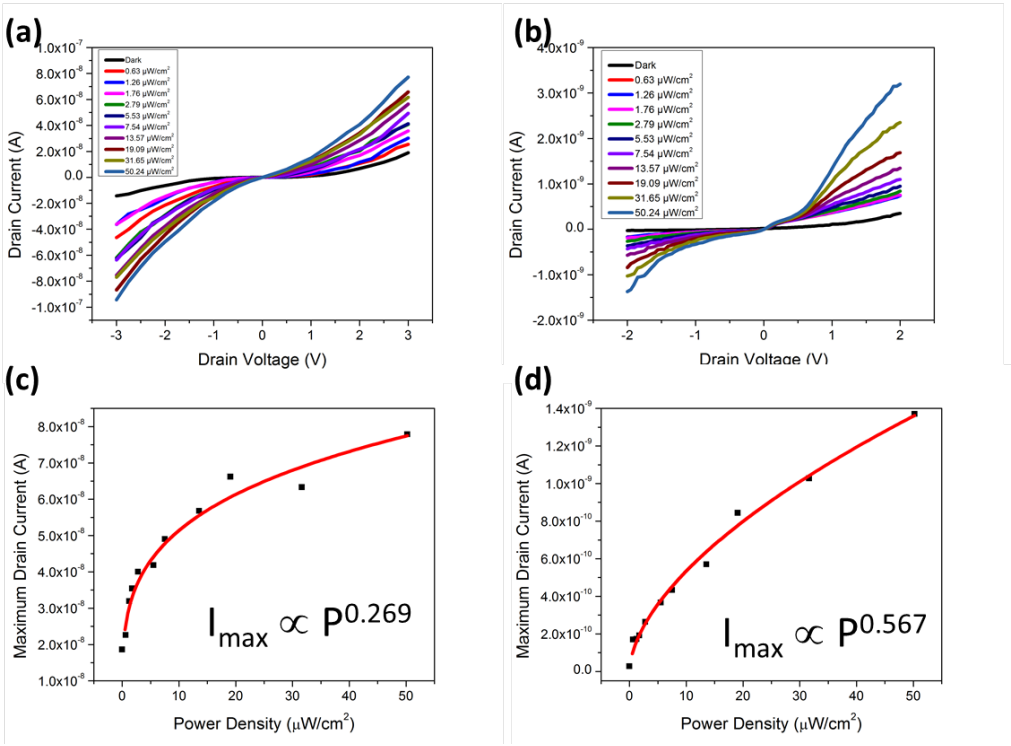

Figure 3.5: I-V curves indicating increased conduction of (a) nanowire and (b) nanosheet devices at increased power intensities. Maximum current of (c) nanowire and (d) nanosheet devices, as a function of optical power density. Note: Red line fits data to a power law distribution and a smaller non-unity exponent refers to a greater abundance of traps and recombination centers

μm), V_{ds} is the applied drain-source voltage, and C_g is the gate capacitance. The gate capacitance was modeled by the expression $C=2\pi\epsilon_0\epsilon_{SiO2}L_g/ln(t_{ox}+r)/r)$, where ϵ_0 and ϵ_{SiO_2} are the vacuum dielectric constant and the dielectric constant of SiO_2 (3.9) respectively, t_{ox} is the oxide thickness of the SiO_2 thermally deposited on the substrate (200 nm), and r is the radius of the nanowire, determined from SEM. The transconductance, gate capacitance, and field effect mobility were determined to be 1.5 nS, 0.497 fF, and 1.51 cm^2/V-s, respectively, for nanowires. The transistor metrics of the nanosheet device employed a slightly altered model with with $\mu_{FE} = g_m L/(WV_{ds}C_0)$ where C_0 is the capacitance per unit length, and W is the device width (10 μm). C_0 is defined, in this case, as $C_0 = \epsilon_0\epsilon_{SiO2}/t_{ox}$. This model is typically found in the analysis of nanoribbon and nanobelt devices (Li *et al.*, 2010c; Wu *et al.*, 2012,

2014) due to their planar, rather than cylindrical, surfaces. For nanosheet devices, the transconductance, linear gate capacitance, and field effect mobility were determined to be 212.74 nS, 17.3 nF/cm, and 4.11 cm^2/V-s. The carrier concentration for both devices was modeled using the expression n=$1/\rho\mu$q, where ρ is the device resistivity (2.06×10^3 Ω-cm, 10.56 Ω-cm for nanosheets) and was found to be 2×10^{15} cm^{-3} for nanowires and 1.44×10^{17} cm^{-3} for nanosheets. [Not sure about this] Previous reports on bulk ZnTe have also indicated that the occupancy of charge centers can change with illumination, and reduce the effective scattering charge(Fischer *et al.*, 1964), which plays a larger role as the size of the crystal reduces into the nano-scale. This may explain the discrepancy in field effect mobility between the two nanostructures. Lastly, subthreshold swing (S) was analyzed for both device sets by S=ln(10)d(V_g)/d(ln(I_{ds})). The subthreshold swing is an important device metric that is a measurement of the devices' switching capability. It was found to be 4.469 V/dec for nanowires and 24.196 V/dec for nanosheets. A comparison of these device metrics have been outlined against previous reports of ZnTe-based nanostructure devices in Table 1.

From this analysis, it is found that the on/off ratio and field-effect mobility among the two device types are quite comparable, with a slight advantage for nanosheets. Although nanosheet devices clearly have a much larger transconductance than those composed of nanowires, the gains in mobility are offset by a gate capacitance that is much larger. This is due to geometric considerations and the overall size of our nanostructures, the W/L ratio of nanosheets far exceeds the inverse of the natural logarithm of the nanowire radius.

Under the illumination of a 532 nm green laser, a set of two terminal measurements of both devices structures were also conducted. The drain-source current response to varying light intensities, ranging from 1.7 to 50.24 W, is shown in Figure 3.5(a).

Device Structure	R_λ (A/W)	Photo-conductive Gain	NEP ($WHz^{-.05}$)	D^* ($cmHz^{0.5}W^{-1}$)
ZnTe NW (Cao *et al.*, 2011b)	2.17×10^3	1.54×10^4	n.a.	n.a.
ZnTe NW (Liu *et al.*, 2013a)	1.87×10^5	4.36×10^5	n.a.	n.a.
ZnTe NW (Li *et al.*, 2010c)	360	8.64×10^3	n.a.	n.a.
ZnTe:Sb nanoribbon (Wu *et al.*, 2012)	4.80×10^4	1.20×10^5	7.5×10^{-17}	4.8×10^{13}
ZnTe NW (this work)	2.62×10^5	6.11×10^5	2.99×10^{-19}	1.10×10^{16}
ZnTe nanosheet (this work)	110.6	257.76	9.96×10^{-17}	2.24×10^{14}

Table 3.2: Comparison of ZnTe nanostructure-based photodetector performance metrics

As compared to measurements collected under dark conditions, a current increase at the maximum operating voltage (3 V) of 3x is observed at maximum illumination power (photocurrent increases from 77.2 nA to 1.89 nA) for nanowires, and 9x at an operating voltage of 2 V for nanosheets. The inset in each plot shows the response of the maximum photocurrent to power density for both nanostructures. For semiconductor photoconductors, this relation has typically exhibited a power law dependence(Rose, 1963) according to $I_{max} \propto P^{\theta}$. By fitting the experimental photocurrent data to the above expression, we arrive at $\theta = 0.2693$ for nanowires and $\theta = 0.5665$ for nanosheets.

A fractional, non-unity exponent is indicative of a continuous distribution of states

(in this case, traps) that convert into recombination centers as the quasi-fermi level shifts due to illumination power. In our analysis, nanowires have a smaller exponent than nanosheets, which suggests a higher abundance of traps. The morphology and size configuration of NWs are more surface-dominated than the nanosheet. As described in previous studies, semiconductor nanowire photodetectors owe their photoconductive properties to surface trap states, and this will becomes more evident upon comparing their photoconductive gains.

The spectral responsivity (R_λ) and photoconductive gain (G) are key figures of merit that distinguish detector systems, and can be defined by the following relationships:

$$R_\lambda = \frac{\Delta I}{PA} \text{ and } G = \left(\frac{\Delta I}{e}\right) / \left(\frac{P}{h\nu}\right)$$

where ΔI is the difference between the photocurrent and dark (resistive) current, P is the irradiation power, A is the area impinged by photons on the top surface of the nanostructures, $h\nu$ is the bandgap energy, and e is the elementary electronic charge. Theoretically, responsivity can also be expressed in terms of the photoconductive gain, which can also be scaled based on the theoretical quantum efficiency by $R_\lambda = q\eta G/h\nu$, where η is the quantum efficiency defined as $\eta = \eta_i(1 - R_{ref})(1 - e^{\alpha d})$. In this expression, η_i is the intrinsic quantum efficiency (assumed to be 1), d is the absorption depth (diameter for nanowires, thickness for nanosheets), and finally R_{ref} and α are the reflectivity and absorption coefficient of ZnTe (assumed from ZnTe-bulk literature data to be 0.278 and $10^5 cm^{-1}$), respectively. In this study, a responsivity of 2.62×10^5 A/W was calculated for nanowires and 110.59 A/W for nanosheets, at their respective operating voltages. Accounting for the theoretical quantum efficiency, the photoconductive gains were calculated to be 6.10×10^5 for nanowires and 257.76 for nanosheets. Another set of metrics characterizing noise in photodetectors systems include the noise equivalent power (NEP) and detectivity

(D^*). These metrics distinguish the sensitivity of detectors, and highly sensitive detectors tend to exhibit low NEP and high D^*. Assuming a shot noise-limited relationship (as shot noise is influenced by the devices' dark current, which, in this case, exceeds Johnson noise), they are calculated as NEP = $(1/R_\lambda)(2qI_d+4kT/R_v)^{1/2}$ and $D^* = (Af)^{1/2}/NEP$, where k is Boltzmann's constant, T is the absolute ambient temperature, I_d is the dark current at the specified operating voltages (18.6 nA for nanowires, 0.352 nA for nanosheets), R_v is the device differential resistance (87.6 MΩ for nanowires, 1.92 GΩ for nanosheets), and f is the amplifier bandwidth (1 kHz).(Sze and Ng, 2006) NEP has been calculated to be 2.99 × 10^{-19} $WHz^{-.05}$ for nanowires and 9.96 × 10^{-17} $WHz^{-.05}$ for nanosheets, and D^* was found to be 1.10 × 10^{16} $cmHz^{0.5}W^{-1}$ for nanowires and 2.24 × 10^{14} $cmHz^{0.5}W^{-1}$ for nanosheets. Table II compiles detection and noise metrics for a variety of ZnTe nanostructure, thin film and bulk systems, as well as other material systems.

As discussed extensively in ZnO nanowire photodetector studies (Soci *et al.*, 2007b; Yu *et al.*, 2012), and as has been adapted to ZnTe nanostructure systems by Cao et al., the adsorbtion and desorbtion process of O_2 along the surface of these materials form traps states from dangling bonds(Cao *et al.*, 2011b). As the nanostructures are illuminated with a photonic energy greater than the bandgap, this process induces the generation of electron-hole pairs, of which electrons tend to create O^- ions along the surface, thereby increase the number of unpaired holes. In our previous discussion, we found that our ZnTe nanostructures exhibit p-type conduction. Thus, as the applied voltage across the channel increases, a hole accumulation layer is formed along the surface with reduced band bending. This results in increased conductivity. In our analysis, we find that the ZnTe nanowires tend to have a much larger responsivity and photoconductive gain than their nanosheet counterparts. We can therefore assume that nanowires have a greater number of traps than nanosheets, which is confirmed by

our previous analysis of their smaller exponent in the power law relationship relating power flux to photocurrent. The geometry of our nanowires also demonstrates a larger surface-to-volume ratio as compared to nanosheets, which indicates that the proposed activity along the surface has a much larger impact on the overall conductive response of our devices. Lastly, we also know that photoconductive gain is traditionally defined as G=τ/τ_{tr}, where τ is the carrier lifetime and τ_{tr} is the transit time between contact electrodes. Hole diffusion is more limited for nanowires, because they have a much more confined active area than nanosheets. A consequence of this is that holes in nanowires can remain mobile for much longer before they are collected at the electrode or recombine in trap states. As the difference transit time for both nanostructures is negligible, this could further explain the larger photoconductive gain observed in ZnTe nanowires. Previous reports which have studied the rise and decay time from illumination in ZnTe nanostructures have confirmed that the size effect has a pronounced impact on carrier lifetime, namely an increase by orders of magnitude (Cao *et al.*, 2011b; Liu *et al.*, 2013a). Thus, the high responsivity, photoconductive gain, and detectivity make the ZnTe NW a more promising optoelectronic option than the nanosheet.

3.5 Conclusion

ZnTe nanostrucutres, including long nanowires and wide nanosheets have been synthesized and their performance as field effect transistors and photodetectors have been analyzed. A Schottky barrier with Cr/Au was uncovered, and a barrier height was determined to be 0.48 eV for nanowires and 0.69 for nanosheets. The devices exhibited hole conduction with comparable field effect mobilities of 1.51 cm^2/V-s for nanowires and 4.11 cm^2/V-s for nanosheets, with nanosheets demonstrating a substantially higher subthreshold swing. The mechanism for nanosheet formation in the

ZnTe material system has been discussed, and the growth related defect chemistry giving rise to p-type behavior has been elaborated upon. The electrical response of nanostructures were also investigated with the illumination of a 532 nm green diode laser. Nanowire devices exhibited a responsivity of 2.62×10^5 A/W, a photoconductive gain of 6.10×10^5, and a power dependence to light intensity with an exponent of 0.269. Likewise, the nanosheet responsivity, photoconductive gain, and power distribution exponent were 110.59 A/W, 257.76, and 0.567, respectively. Additionally, the noise parameters, NEP and D* of the devices have been calculated to be 2.99×10^{-19} $\mathrm{WHz}^{-.05}$ and 1.10×10^{16} $\mathrm{cmHz}^{0.5}\mathrm{W}^{-1}$ respectively, for nanowire-based ZnTe devices, and 9.96×10^{-17} $\mathrm{WHz}^{-.05}$ and 2.24×10^{14} $\mathrm{cmHz}^{0.5}\mathrm{W}^{-1}$ for nanosheet-based ZnTe devices. These results indicate that nanowires owe their superior photoconductive performance to their extremely small geometry, leading to a higher surface-to-volume ratio. This makes the effect of trap states more pronounced for nanowires, leading to longer carrier lifetimes than that nanosheets.

Chapter 4

SYNTHESIS AND CHARACTERIZATION OF ZNO/ZNTE CORE/SHELL MICROSTRUCTURES

4.1 Abstract

Direct band gap II-VI nanowire-based semiconductors are attractive for photonic applications owing to their appeal to the capability of modulating optoelectronic properties of the material and relative ease and low cost of synthesizing. A core-shell configuration of intrinsic n-type Zinc Oxide (ZnO) and p-type Zinc Telluride (ZnTe) hetero-nanowires were studied for applications in photovoltaics. In this work, the ZnO/ZnTe heterojunctions were fabricated via vertically aligned, high-quality, low-defect ZnO nanowires (200 nm diameter and 5 μm length) grown on a low resistance Si (100) substrate using a high temperature vapor-liquid-solid (VLS) deposition at 700 °C and the ZnTe shell was subsequently grown using a lower temperature VLS deposition chamber. The thickness was increased until a hybrid structure was formed. The deposition of ZnTe on ZnO nanowires can be controlled through the growth temperature, and their morphology was examined by scanning electron microscope. TEM analysis was not able to confirm ZnTe deposition due to the strengh of the ZO signal. However, the presence of ZnTe was confirmed using EDX mapping, XRD, and photoluminescence measurements. At Raman modes specific to ZnTe, no ZnO signal was discerned. Furthermore, light scattering measurements illustrated attenuation related to ZnTe and ZnO band edge wavelengths. Additionally, the longer time scale for carrier lifetimes illustrated by the time-resolved photoluminescence measurements indicated that the ZnTe/ZnO interface created was type-II staggered in nature. A

top contact was formed by sandwiching indium tin oxide (ITO) covered glass over the hybrid nanowire array and using the Si substrate as a bottom contact, thereby characterizing photovoltaic response. The devices exhibited low power conversion efficiency due to recombination centers contributing to loss.

4.2 Introduction

One-dimensional semiconductor nanowires arrays have garnered incredible interest due to potential advanced optoelectronic applications, especially through vertical integration in solar cell applications that can extend carrier lifetimes. Among these is ZnO, a material that preferential n-type conductivity, with a bandgap of 3.37 eV limited to UV range absorption. Many techniques have been employed toward using smaller band gap materials to expand the absorption, which allows for increased light harvesting and overall energy-conversion efficiency of the solar cell. One of the most popular methods is fabricating core/shell structure by coating ZnO NWs with a uniform thin film shell of the II-VI group of materials (Tak *et al.*, 2009; Leschkies *et al.*, 2007). The core/shell type-II heterojunction between the ZnO nanowires and

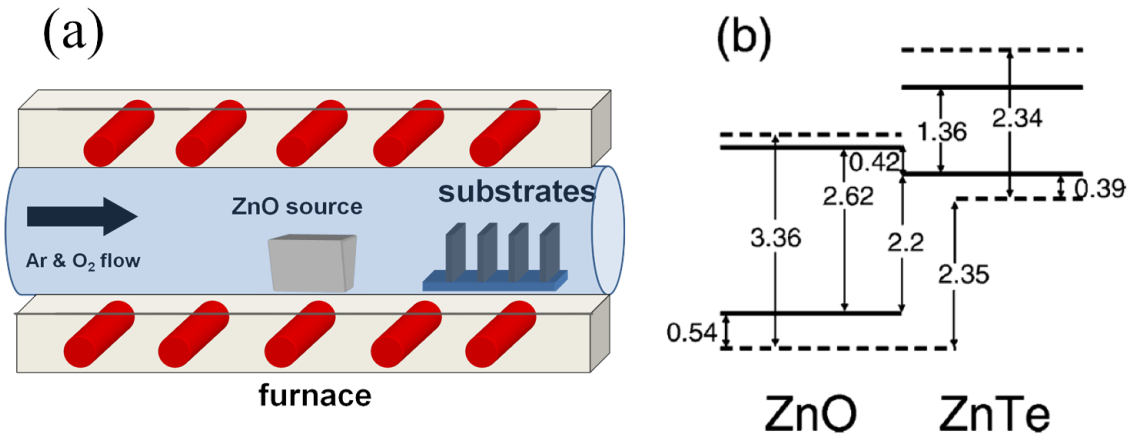

Figure 4.1: (a) Experimental Growth Setup for ZnO nanowires (b) Calculated VBM and CBM alignments for ZnO/ZnTe core/shell structure

the shell material radially surrounding lead to effective charge separation with the shell acting as an absorber or generation site and the nanowire core as an electron transporter (Leschkies *et al.*, 2007; Lévy-Clément *et al.*, 2005). Among the most interesting materials that can form a type-II band alignment with ZnO is ZnTe, another II-VI semiconductor material that can potentially extend the absorption range to 1.17 eV, and also exhibits preferentially p-type conduction. Forming a p-n heterojunction interface between the two materials has been studied extensively theoretically and experimentally, and have reported benefits to solar cell performance. In this work, high-quality, single crystalline ZnO/ZnTe core shell structures have been synthesized with a two-step process involving ZnO nanowire formation and ZnTe coating with vapor phase deposition method. The structures have been studied before and after ZnTe deposition with regards to scanning electron microscopy (SEM), energy dispersive x-ray spectroscopy (EDX) mapping, transmission electron microscopy, Raman spectroscopy, light scattering and time-resolved photoluminescence. The results confirm conformal coating of ZnO nanowires with ZnTe and a type-II staggered band alignment.

4.3 Experimental Details

Aligned ZnO nanowires were vertically synthesized using a typical vapor-solid growth furnace. ZnO powder mixed with graphite at 1:1 molar ratio was placed at the 1100 °C. A ZnO sputtered growth substrate was placed in a vertical sample holder, while Argon was used as a carrier gas with a flow rate of 110 sccm along with 10 sccm of oxygen. A schematic diagram of ZnO nanowire growth set-up illustrating a single-zone quartz tube furnace containing ZnO source and growth substrates is shown in Figure 4.1(a). The Ar and O_2 gas are introduced from the inlet of the furnace and ZnO source mixed with graphite powder is placed in the center of the furnace so that

ZnO is vaporized and deposited onto the substrates placed downstream at varying temperatures.

The result under electron microscopy (SEM) was an ordered array of ZnO nanowires with aligned vertical orientation. Using a similar vapor transport technique, ZnTe powder was vaporized and deposited on the vertical ZnO pillars using a lower temperature (due to the transition temperature of ZnTe). Heteroepitaxial structures were then formed over the ZnO, and in some cases, evidence of film coverage were observed. Scanning electron microscopy was again conducted, this time on the resulting coarse structures. The material was also characterized with EDX mapping and TEM.

4.4 Results and Discussion

The synthesis and morphology of ZnO nanowires have been investigated, are illustrated in Figures 4.2 for the top view and Figure 4.3 for the cross-sectional view. Based on the furnace temperature profile, ZnO nanowires grown between 1000 °C and

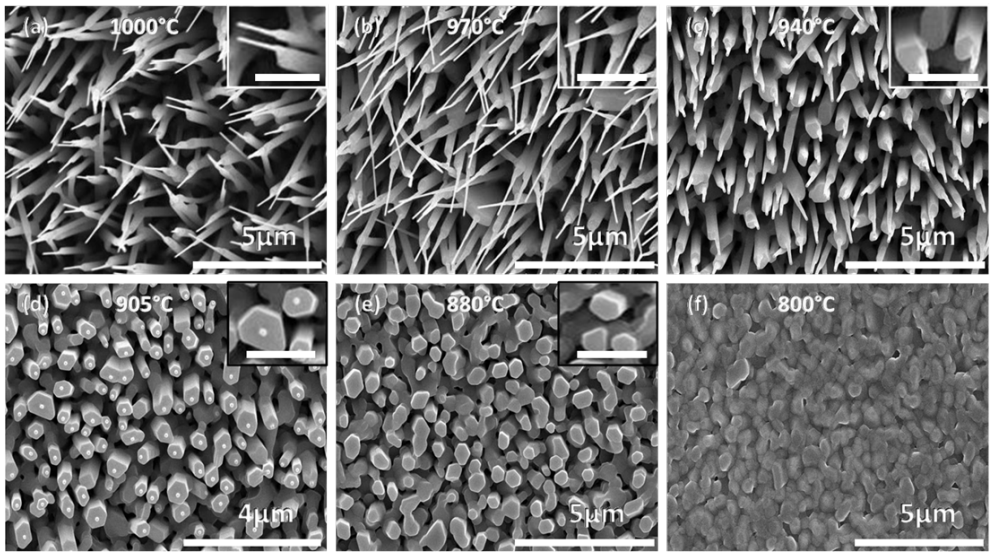

Figure 4.2: FESEM images (top-view) of ZnO nanowires with the growth temperature; (a) 1000 °C, (b) 970 °C, (c) 940 °C, (d) 905 °C, (e) 880 °C, (f) 840 °C, (g) 800 °C. The scale bar of all the inset images between (a), (b), (c), (d), and (e) is 1.25 μm, 1.25 μm, 1.25 μm, 1 μm, 1.25 μm, respectively

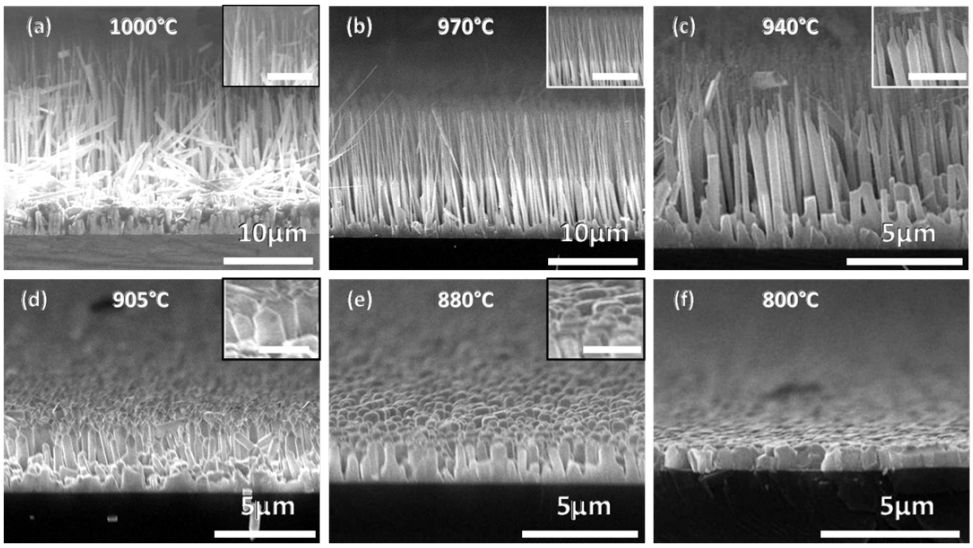

Figure 4.3: FESEM images (cross-sectional view) of ZnO nanowires with the growth temperature; (a) 1000 °C, (b) 970 °C, (c) 940 °C, (d) 905 °C, (e) 880 °C, (f) 840 °C, (g) 800 °C. The scale bar of inset images between (a), (b), (c), (d), and (e) is 2.5 μm, 2.5 μm, 1.25 μm, 1.25 μm, 1.25 μm, respectively.

900 °C form thicker base with thin shallow tip on this base rod while those grown below 900 °C form thick and wide film. The nanowires grow vertically and are well aligned and exhibit a hexagonal morphology typical of wurtzite crystal structure. They were measured with an average of 5 μm in length and 300 nm in diameter. Local temperature was found to be a major determinant in the morphology of ZnO grown. At a lower temperature, ZnO is retains liquid form for a shorter period and assembles at a slower rate. The opposite is true at a higher temperature. The inclusion of oxygen in this process is also an important determinant in the dimensions and composition of the wire grown. Without sufficient oxygen, Zn^{2+} ions form bonds with themselves and create zinc metals that condense along the growth chamber wall (Wang, 2007). With larger temperatures and larger thermal energies, the energy exceeds the bonding energy of O_2, which does not allow it to remain as a diatomic (Ozgur *et al.*, 2005). With decreased thermal energy, O_2 ions are able to transport away from the source region, and thereby bond with lone Zn^{2+} ions (Wang *et al.*,

2007). Thus, a multizone furnace is used to extend across a range of temperatures to create the desired feature and stiochiometric composition of ZnO.

In Figure 4.4, the scanning electron micrograph is presented for ZnO nanowires, before and after coverage with ZnTe. Post deposition of ZnTe, the ZnO nanowires exhibited a conformal, rough coating of dissimilar crystal grain. The top micrograph illustrates a controlled deposition time in the reaction limited regime that allow for conformal coating of the ZnO nanowire. In this case, the nanostructure retains in morphology, but in the case of a diffusion-limited regime, the ZnO nanowire arrays are completely subsumed by a ZnTe thin film. Regime limitation of deposition was controlled by temperature in this case, and plays a major role in producing blanket coverage films over coatings.

Figure 4.5 illustrates the EDX mapping of a select subset of core/shell ZnO/ZnTe nanowire structures, in which the degree of elemental content is signaled by color and brightness over the raster image. The Te signal alone forms an indistinguishable

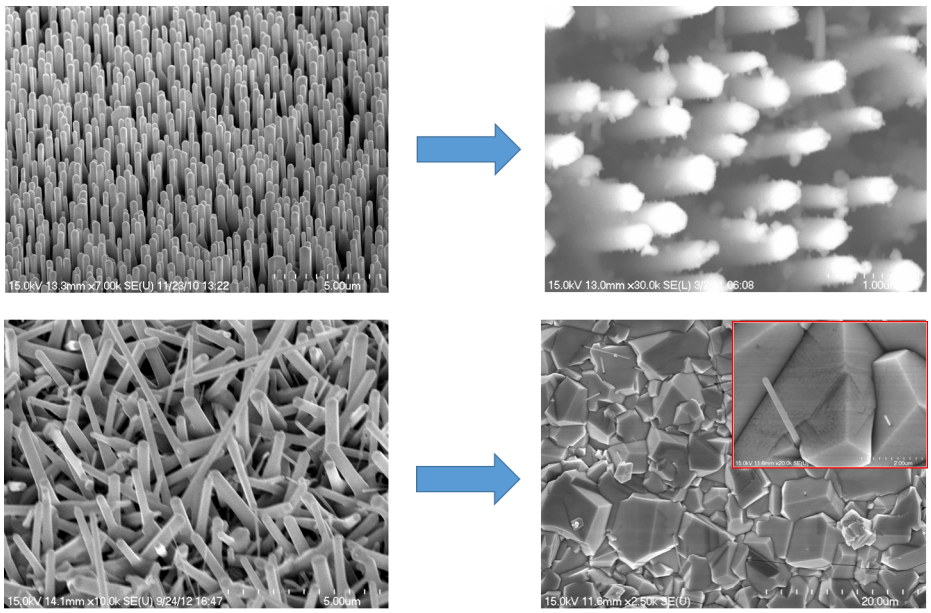

Figure 4.4: SEM Micrograph of ZnO/ZnTe core shell (a) before and (b) after ZnTe deposition

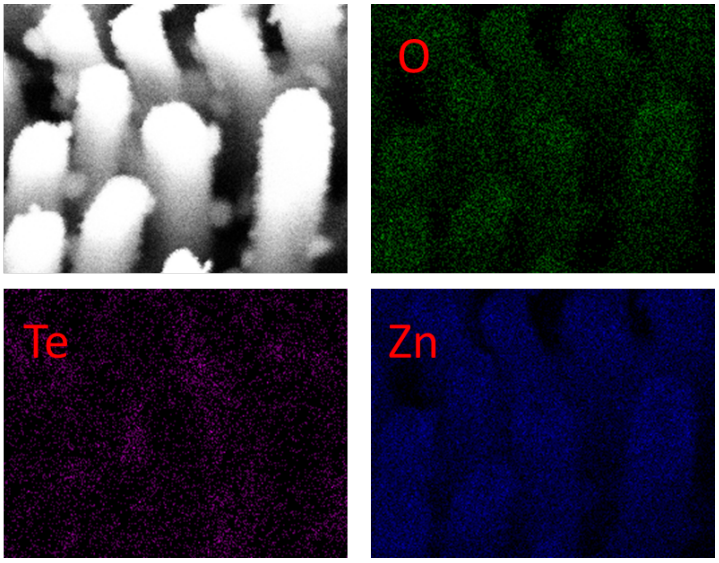

Figure 4.5: EDX Mapping of ZnO/ZnTe core shell nanostructure

feature as a nanowire, as compared to the strongly defined Zn signal. These results confirm homogeneous, conformal coverage of ZnTe over the ZnO core through the uniform distribution of ZnTe on the surface.

Figure 4.6 shows the transmission electron micrograph of ZnO/ZnTe core/shell nanowires. Due to the large diameter of sampled nanostrucutre, electrons could not penetrate, leaving only information on ZnO lattice structure. This is due to the oxidation of ZnTe shell, leaving a thin ZnO layer. The diffraction pattern resolved from the TEM illustrates lattice spacing consistent with ZnO.

XRD patterns were obtained to differentiate the crystal structures of ZnO and the ZnO/ZnTe core/shell array, and are shown in Figure 4.7. The diffraction peak typical of ZnO (002) is observed at 34.2°, pre-deposition of ZnTe, and the dominant ZnO peak of (002) planes reveals that the ZnO nanowires were grown with a c-axis orientation normal to the substrate surface. After the deposition of ZnTe shell layer, we find additional ZnTe related peaks from the (111), (220), and (311) zinc blende planes of ZnTe at 25.26°, 41.8°, 49.5°respectively. Additionally, the 2θ position of ZnO (002) was observed to shift slightly to the smaller angle side (inset), indicating

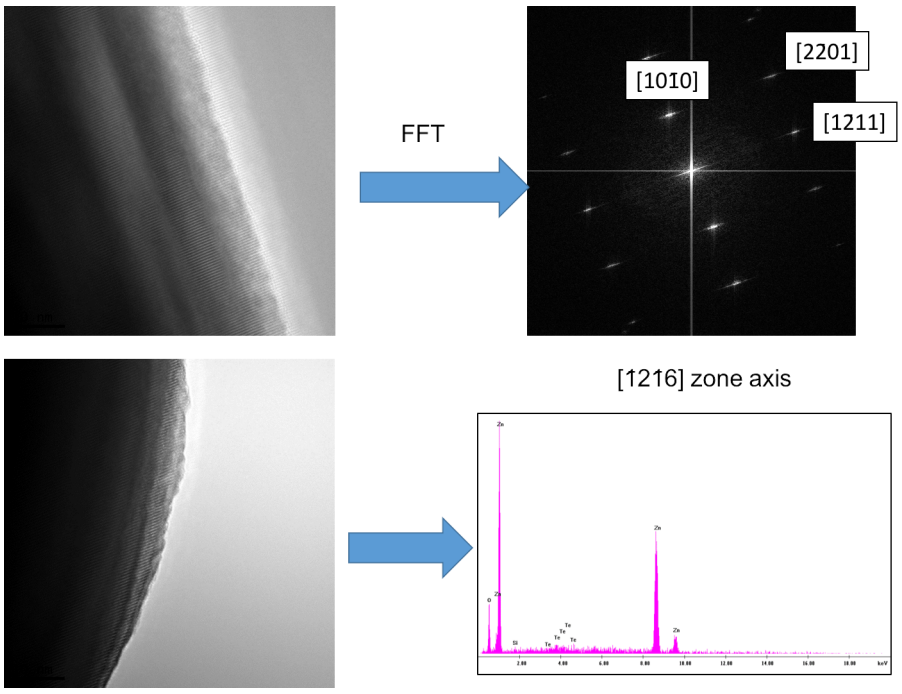

Figure 4.6: TEM Micrograph of ZnO/ZnTe core shell (a) before and (b) after ZnTe deposition

that ZnO has experienced a lattice expansion due to the ZnTe shell growth. The enlarged ZnO lattice was also observed after the deposition of ZnSe layer on ZnO nanowires by Mascarenhas et al.

The Raman spectra of ZnO wires from the range of 180-480 cm^{-1} are shown in Figure 4.8 (a). The predominant peak is found of that for the ZnO E2 (high) at 437 cm^{-1}, which suggest good crystal integrity of ZnO. The related Raman modes of ZnO wires are shown in Table 4.1. Post ZnTe deposition, the dominant peaks are found to be that of ZnTe at 214 , 420, 625, 830 cm^{-1} (Figure 4.8b), indicating the 1LO(Γ), 2LO(Γ), 3LO(Γ) and 4LO(Γ) modes of ZnTe respectively. These results indicate the ZnTe was appropriately deposited over the ZnO arrays forming highly crystalline core/shell arrays.

Figure 4.9 shows the spectrum for Raman mapping and the inset shows the images of ZnO/ZnTe structure under the microscope. The red rectangle shows the scanned

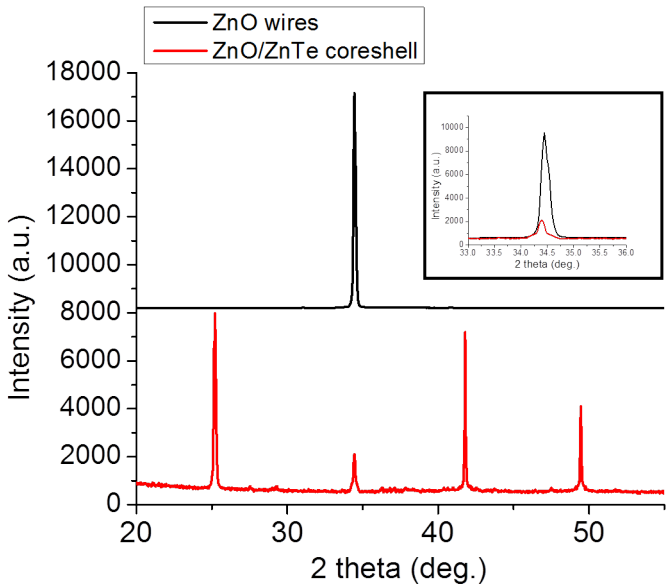

Figure 4.7: XRD pattern of ZnO and ZnO/ZnTe core/shell arrays

area for Raman mapping. Further Raman analysis was conducted by integrating the modes of 425-440 cm^{-1} for ZnO, 200-220 cm^{-1} for ZnTe, 300-430 cm^{-1} for ZnTe and 615-640 cm^{-1} for ZnTe, shown in Figure 4.10. It is noted that the ZnO related mode is found to attenuate post-deposition, which further indicate the successful incorporation of ZnTe as a shell to ZnO.

To understand the light absorption properties of the ZnO/ZnTe core shell structure, a light scattering measure mention was conducted on ZnO nanowire arrays before and after ZnTe incorporation. Pre-deposition, there appears to be absorption in the visible range, until the energy band level of ZnO is obtained, shown in Figure 4.11. For the core/shell structure, there are two predominant attenuation points related to the band gap of both ZnO and Znte (370 nm and 550 nm, respectively). Reflection intensity is also found to decrease at a decreasing rate between the two wavelengths. Assuming that the composite structure exhibits a smaller bandgap and a staggered type-II band alignment that is of lesser magnitude that the individual materials alone, this could be confirmation of such a phenomena, as it is near the

Raman mode	E_2-low	2TA $2E_2$-low	2TA(X) (Si)	2-E_2(M)	E_1-TO	E_2-high
1000 °C	102.1	207.5	N/A	333.4	387.8	438.8
970 °C	100.5	207.5	N/A	331.9	395.6	437.2
940 °C	102.1	N/A	N/A	331.9	403.3	438.8
905 °C	102.1	N/A	308.4	330.3	N/A	437.2
880 °C	102.1	N/A	302.1	331.9	N/A	437.2
840 °C	102.1	N/A	303.7	N/A	N/A	437.2
800 °C	102.1	N/A	300.6	N/A	N/A	437.2

Table 4.1: Temperature Evolution of Raman modes of ZnO wires

theoretical bandgap of 1.2 eV. The smaller net reflection intensity for the core/shell structure, compared to ZnO alone suggests that the core/shell structure is more adept at light trapping. These step from the grains on the surface of the wire which create multiple sites of reflection and light absorption, which are beneficial for photovoltaic applications.

The photoluminescence spectra of ZnO and ZnTe core/shell structures is illustrated in Figure 4.12. In the case of ZnO, peaks along the 370 nm band edge (due to recombination of free excitons), along with a broad red emission at 630 nm (due to recombination of delocalized electrons near the conduction band with deeply trapped holes in the negatively charged interstitial oxygen ion center) are observed, and similarly to reported elsewhere. The intense 370 nm ultraviolet peak indicates excellent crystallinity with low defect concentrations. When ZnTe is deposited, a broad peak centered at 630 nm and ranging over 500-800 nm is observed, due to the oxygen defect on ZnTe. The emission of both ZnO and ZnTe were found to attenuate emission intensity. This is attributed to the modified band alignment which stems from ZnTe

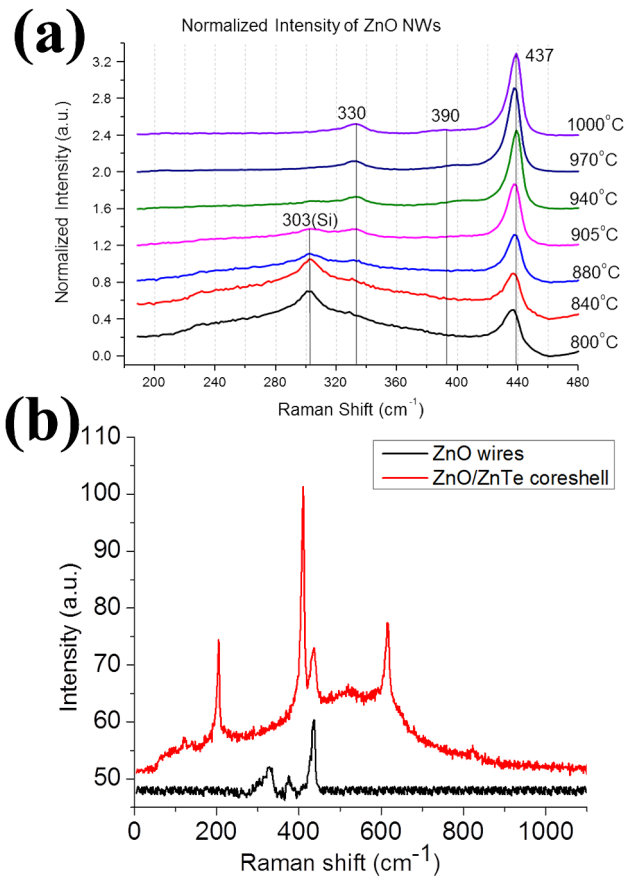

Figure 4.8: Raman spectra of (a) ZnO and (b) ZnO/ZnTe core/shell arrays

promoting charge separation over the staggered gap.

Time-resolved photoluminescence (TRPL) is a technique commonly utilized to examine the decay dynamics leading to the determination of the lifetime of the excited electron-hole pair. The lifetime of photoluminescence is the average time for the excited carriers to stay in the excited state between the photo-excitation and photon emission. TRPL spectroscopy is used to study the radiative or nonradiative lifetimes of the ZnO/ZnTe core/shell structure. The TRPL intensity as a function of time is expressed in an exponential decay relationship as the following formula:

$$I(t) = I_o e^{-t/\tau} \tag{4.1}$$

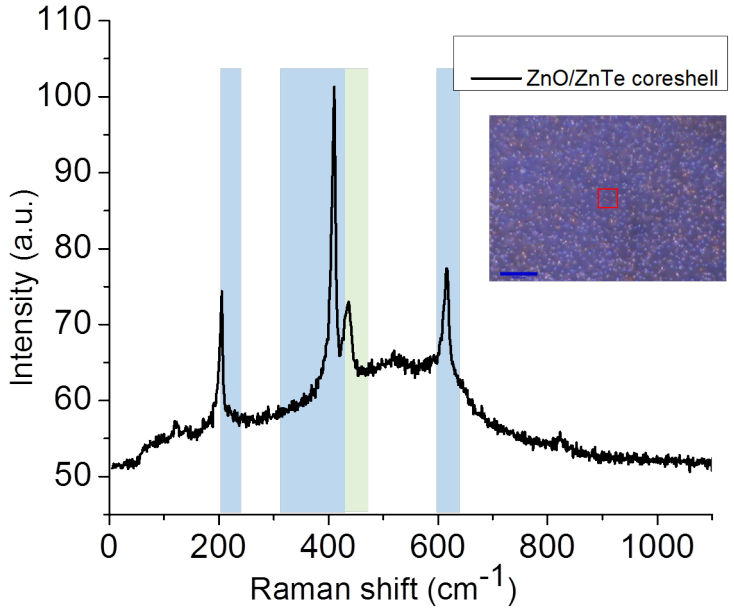

Figure 4.9: Scanned Raman spectrum for Raman mapping. Highlighted regions indicate ranges examined

where I_o is the initial intensity, t is the time and τ is the recombination time. Analyzing the spectra as a function of time allows the recombination time to be extracted. One essential difference between type-I and type-II semiconductors is the recombination time or lifetime of the PL. Because of the spatial separation of holes and electrons, type-II semiconductors have considerably longer lifetimes (on the order of 1 - 100 ns) (Lin et al., 2008; Weisbuch et al., 1991; Najjar et al., 2009) when compared to type-I semiconductors (10 - 100 ps) (Weisbuch et al., 1991). TRPL measurements of InGaN MQW (type-I) shows lifetime smaller than 2000 ps. (Pophristic et al., 1999) Najjar et al. reported TRPL measurements having lifetime of 5ns for ZnSe/ZnTe QDs (Pophristic et al., 2009). Lin et al., reported TRPL measurements showing lifetime of 21 ns (Lin et al., 2006).

Figure 4.13 shows the Time-Correlated Single Photon Counting (TCSPC) result of kinetic traces at 450, 500, 550, 600 nm with excitation 405 nm.The extracted

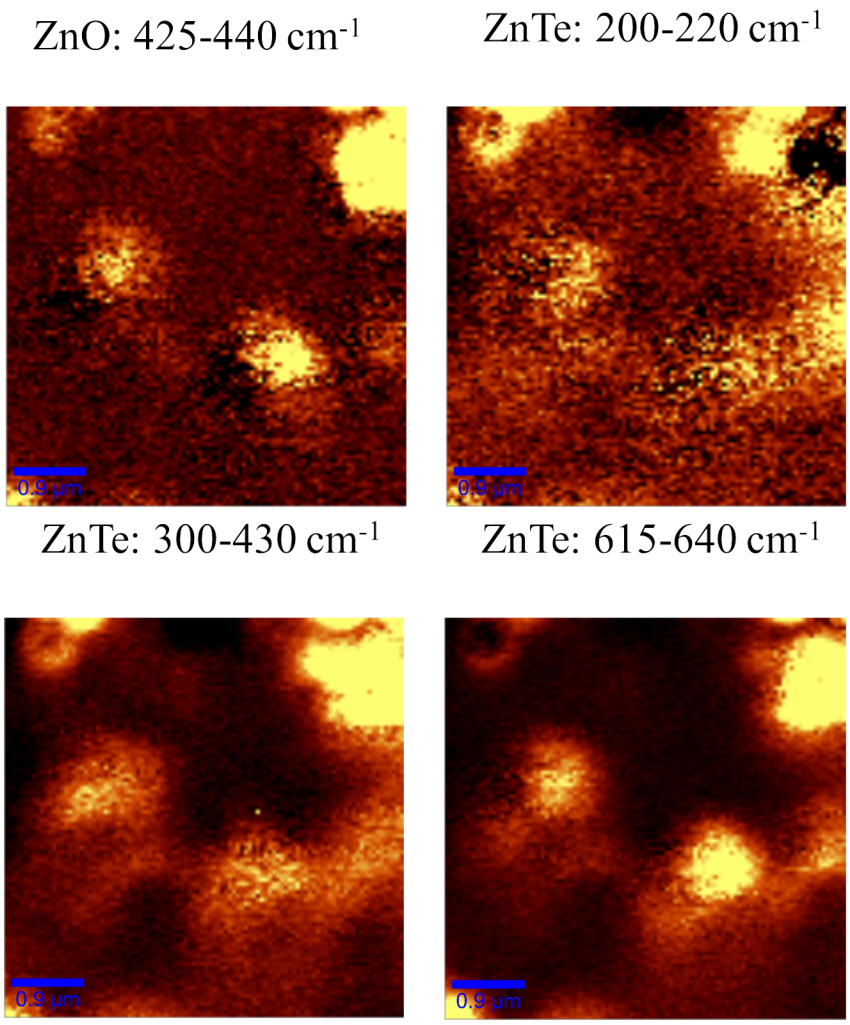

Figure 4.10: Raman mapping of (a) ZnO and (b-d) ZnO/ZnTe core/shell arrays

lifetime is 3-4 ns, which does not change with the probe wavelength. Compared to the lifetime of type-I semiconductors (10 - 100 ps), ZnO/ZnTe core/shell structure has relative long lifetime showing an indication of type-II transitions.

Current-voltage measurements were also conducted vertically on the ZnO/ZnTe structures, as shown in Figure 4.14. We note that the structure exhibits non-rectifying behavior, which indicates that the contact selection may be ohmic in nature. However, a slight current-voltage profile shift is exhibited, with a corresponding open circuit voltage and short circuit current, which suggests a slight degree of photovoltaic

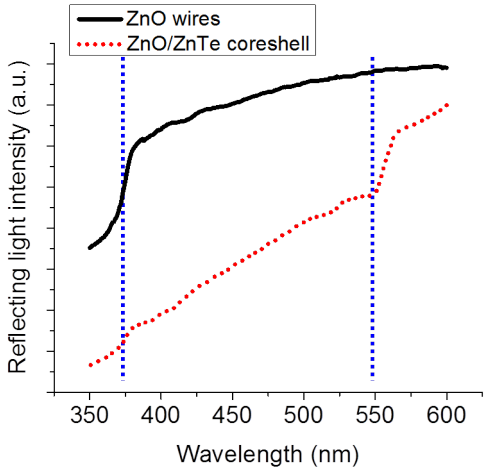

Figure 4.11: Light scattering of ZnO and ZnO/ZnTe core/shell arrays

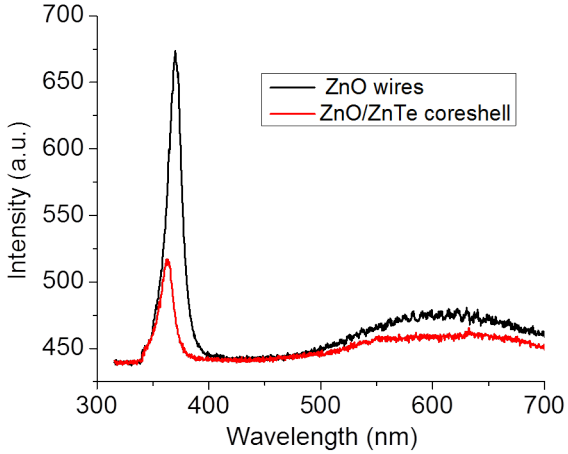

Figure 4.12: Photoluminescence of ZnO and ZnO/ZnTe core/shell arrays

behavior.

4.5 Conclusion

In this work, ZnO/ZnTe core/shell vertically aligned nanowire arrays have been demonstrated. SEM analysis shows characteristic rough coating, indicative of ZnTe grains forming on the surface of ZnO nanowires. XRD, PL, Raman, and light scattering confirm the integration of ZnTe on ZnO arrays, and suggest the formation of the

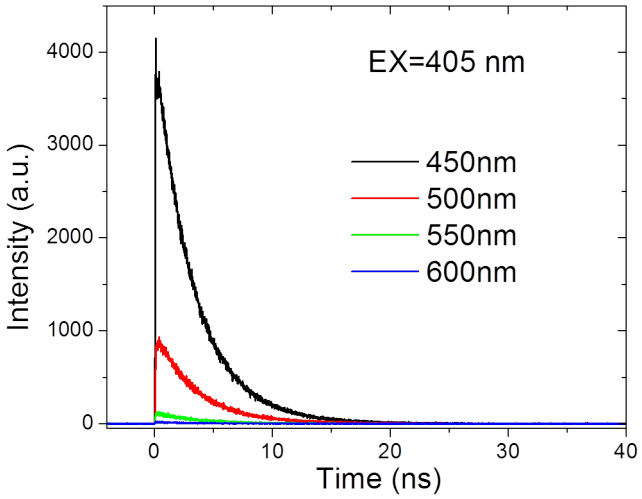

Figure 4.13: Time-resolved photoluminescence of ZnO/ZnTe core/shell structure

type-II staggared band. The use of EDX mapping, XRD, Raman spectroscopy, and photoluminescence was used to confirm the coverage of ZnO with ZnTe. Light scattering confirmed the formation of both crystal structures on the nanostructure lattice. TEM analysis, however, was unable to discern ZnTe-related diffration patterns. Additionally, time-resolved photoluminescence results indicate longer carrier lifetimes, suggesting type-II staggered band alignment achieved between ZnTe and ZnO. With electrical characterization, these material systems may prove to highly impact the power conversion efficiency of such nanowire-based photovoltaics by exploiting the type-II band alignment and dissimilar conductivity between the two semiconductors.

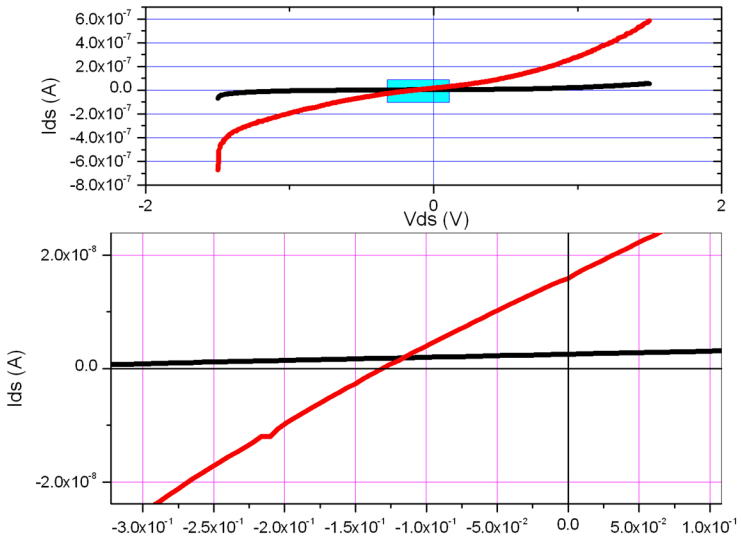

Figure 4.14: Current-Voltage measurement of ZnO/ZnTe core/shell structure. Note: Black trace is dark and red trace is illuminated with AM 1.5G

Chapter 5

CONCLUSION

In conclusion various applications of ZnTe have been demonstrated, stemming from vapor phase growth. The growth of ZnTe was documented, with the growth of polycrystalline films without catalyst and single crystal nanostructures with a catalyst. The different morphologies were controlled through either the absence or the presence of gold (Au) catalyst deposited as a seeding layer on silicon (100) substrates before growth. These results indicate that the ZnTe thin films exhibited polycrystalline structure, and the grains imply a significant size effect, as the mobility of the boundaries increases as the grain size increases. Submicron wires and sheets exhibited single-crystal structures and the preference for the (111) orientation indicates that the crystal preferentially grows via close-packed planes {111} to minimize the surface energy and the peak intensity ratio (550 nm/725 nm) of PL increases with the growth temperature indicated that the growth temperature plays an important role in the crystal quality. The high quality single crystal submicron features, which extend up to several microns in length can facilitate device applications through percolating networks. The vapor deposition approach with the use of Au catalyst, can synthesize ZnTe thin films and submicron structures at low cost.

The nanostructures were then used to create three-terminal devices and two-terminal photodetectors, and their relative transistor and detectivity properties have been assessed. A Schottky barrier with Cr/Au was uncovered, and a barrier height was determined to be 0.48 eV for nanowires and 0.69 for nanosheets. The devices exhibited hole conduction with comparable field effect mobilities of 1.51 cm^2/V-s for nanowires and 4.11 cm^2/V-s for nanosheets, with nanosheets demonstrating a sub-

stantially higher subthreshold swing. The mechanism for nanosheet formation in the ZnTe material system has been discussed, and the growth related defect chemistry giving rise to p-type behavior has been elaborated upon. The electrical response of nanostructures were also investigated with the illumination of a 532 nm green diode laser. Nanowire devices exhibited a responsivity of 2.62×10^5 A/W, a photoconductive gain of 6.10×10^5, and a power dependence to light intensity with an exponent of 0.269. Likewise, the nanosheet responsivity, photoconductive gain, and power distribution exponent were 110.59 A/W, 257.76, and 0.567, respectively. Additionally, the noise parameters, NEP and D* of the devices have been calculated to be 2.99×10^{-19} $\mathrm{WHz}^{-.05}$ and 1.10×10^{16} $\mathrm{cmHz}^{0.5}\mathrm{W}^{-1}$ respectively, for nanowire-based ZnTe devices, and 9.96×10^{-17} $\mathrm{WHz}^{-.05}$ and 2.24×10^{14} $\mathrm{cmHz}^{0.5}\mathrm{W}^{-1}$ for nanosheet-based ZnTe devices. These results indicate that nanowires owe their superior photoconductive performance to their extremely small geometry, leading to a higher surface-to-volume ratio. This makes the effect of trap states more pronounced for nanowires, leading to longer carrier lifetimes than that nanosheets.

Finally, core/shell structures for photovoltaic applications have been explored with future work suggested for achieving high performing solar cells. Notably, this came about from a discussion of ZnO nanowire growth mechanisms that explored the nature of temperature in creating a stiochiometrically pure nanostructure. Furthermore, the conformal coverage of ZnTe was discussed in regards to diffusion versus reaction limited regimes that allowed for ZnTe to conformally coat ZnO nanowires. EDX mapping confirmed the growth of a core shell structure by exhibiting signals related to tellurium and Zn, thereby indicating homogeneous coverage. Unfortunately, due to the strength of the ZnO signal, over ZnTe, TEM analysis was not able discern a proper ZnTe signal, allowing only for the analysis of a ZnO diffraction pattern. XRD analysis revealed peak planes for both ZnO and ZnTe, indicating that ZnO nanowires

grew on a c-axis orientation, and that 2θ peaks related to ZnTe emerged, and modified the ZnO peak, indicating lattice expansion (due to a shift). The Raman spectra of grown core/shell structures were also analyzed, with a strong peak related to the ZnO E2 mode, indicating good crystal integrity. Post-deposition of ZnTe, further modes related to ZnTe emerged indicating crystalline shells of ZnTe, including the first through fourth longitudinal optical modes. Raman mapping indicated successful incorporation of ZnTe due to weakened ZnO related modes, and strengthen ZnTe related modes. Light scattering measurements indicated absorption in the visible range, which suggested that that ZnTe incorporation was successful, as attenuation due to absorption from energies related to the band edge of ZnTe were observed. Furthermore, light-scattering in conjunction with Raman confirmed the formation of a staggered type-II band alignment due to a more immediate drop-off after the ZnO band edge. Photoluminescence analysis showed a broad red band emission due to delocalized electrons near the conduction band, with deep trapped holes in the negatively charged interstitial oxygen ion center. With time-resolved analysis, the lifetime of excited carriers could be assessed in terms of radiative and non-radiatives lifetimes through an exponential decay. This analysis was able to confirm a type-II band alignment due to longer lifetimes, and was also corroborated with time-correlated single photon counting. Finally, current voltage measurements were undertaken to confirm a shifted I-V trace that suggests a slight degree of photovoltaic behavior. We assume that the low power conversion efficiency is related to recombination centers that exist within the interface of deposited ZnTe layers and ZnO.

In conclusion this work shows the broad range of ZnTe nanostructures from fundamental synthesis and morphological variation, to electronic and optoelectronic devices, and finally to a photovoltaic application exploiting type-II staggered band alignment. While this work does not completely revolutionize the applications this material

system could potentially drive, it offers insights from the fundamental growth, electronic properties, and photovoltaic potential allowable from the sets of experiments reported in this dissertation.

BIBLIOGRAPHY

Agarwal, R. and C. M. Lieber, "Semiconductor nanowires: optics and optoelectronics", **85**, 3, 209–215, 00208 (2006).

Amutha, R., A. Subbarayan and R. Sathyamoorthy, "Influence of substrate temperature on microcrystalline structure and optical properties of znte thin films", Crystal Research and Technology **41**, 12, 1174–1179 (2006).

Bacaksiz, E., S. Aksu, N. Ozer, M. Tomakin and A. Ozcelik, "The influence of substrate temperature on the morphology, optical and electrical properties of thermal-evaporated znte thin films", Applied Surface Science **256**, 5, 1566–1572 (2009).

Bae, J., H. Kim, X.-M. Zhang, C. H. Dang, Y. Zhang, Y. J. Choi, A. Nurmikko and Z. L. Wang, "Si nanowire metal–insulator–semiconductor photodetectors as efficient light harvesters", Nanotechnology **21**, 9, 095502 (2010).

Balu, A., V. Nagarethinam, A. Thayumanavan, K. Murali, C. Sanjeeviraja and M. Jayachandran, "Effect of thickness on the microstructural, optoelectronic and morphological properties of electron beam evaporated znte films", Journal of Alloys and Compounds **502**, 2, 434–438 (2010).

Belagodu, T., E. A. Azhar and H. Yu, "Modulation of charge conduction in ZnO nanowires through selective surface molecular functionalization", **4**, 23, 7330–7333 (2012).

Bhunia, S. and D. N. Bose, "Schottky barrier studies on single crystal ZnTe and determination of interface index", Journal of Applied Physics **87**, 6, 2931–2935 (2000).

Bouazzi, A., Y. Marfaing and J. Mimila-Arroyo, "Optimization of graded band gap cdhgte solar cells", Revue de Physique Appliquee **13**, 3, 145–154 (1978).

Bozzini, B., M. A. Baker, P. L. Cavallotti, E. Cerri and C. Lenardi, "Electrodeposition of znte for photovoltaic cells", Thin Solid Films **361**, 388–395 (2000).

Cao, Y., Z. Liu, L. Chen, Y. Tang, L. Luo, J. Jie, W. Zhang, S. T. Lee and C. S. Lee, "Single-crystalline znte nanowires for application as high-performance green/ultraviolet photodetector", Optics express **19**, 7, 6100–6108 (2011a).

Cao, Y. L., Z. T. Liu, L. M. Chen, Y. B. Tang, L. B. Luo, J. S. Jie, W. J. Zhang, S. T. Lee and C. S. Lee, "Single-crystalline ZnTe nanowires for application as high-performance Green/Ultraviolet photodetector", Optics Express **19**, 7, 6100–6108, URL `http://www.opticsexpress.org/abstract.cfm?URI=oe-19-7-6100` (2011b).

Cao, Y. L., Z. T. Liu, L. M. Chen, Y. B. Tang, L. B. Luo, S. T. Lee and C. S. Lee, "In-situ phosphrous doping in ZnTe nanowires with enhanced p-type conductivity", Journal of Nanoscience and Nanotechnology **12**, 3, 2353–2359, 00000 (2012).

Capasso, F., "Compositionally graded semiconductors and their device applications", Annual Review of Materials Science **16**, 1, 263–291 (1986).

Chang, J. H., T. Takai, B. H. Koo, J. S. Song, T. Handa and T. Yao, "Aluminum-doped n-type ZnTe layers grown by molecular-beam epitaxy", **79**, 6, 785–787 (2001).

Cho, J. Y., W. H. Nam, Y. S. Lim, W.-S. Seo, H.-H. Park and J. Y. Lee, "Bulky mesoporous tio 2 structure", RSC Advances **2**, 6, 2449–2453 (2012).

Cui, Y., Q. Wei, H. Park and C. M. Lieber, "Nanowire nanosensors for highly sensitive and selective detection of biological and chemical species", **293**, 5533, 1289–1292, URL `http://www.sciencemag.org.ezproxy1.lib.asu.edu/content/293/5533/1289` (2001).

Cui, Y., Z. Zhong, D. Wang, W. U. Wang and C. M. Lieber, "High performance silicon nanowire field effect transistors", **3**, 2, 149–152, URL `http://dx.doi.org/10.1021/nl0258751` (2003).

Davami, K., H. M. Ghassemi, R. S. Yassar, J.-S. Lee and M. Meyyappan, "Thermal breakdown of znte nanowires", ChemPhysChem **13**, 1, 347–352 (2012).

Desnica, U., "Doping limits in ii–vi compounds-challenges, problems and solutions", Progress in crystal growth and characterization of materials **36**, 4, 291–357 (1998).

Devami, K., D. Kang, J.-S. Lee and M. Meyyappan, "Synthesis of znte nanostructures by vapor-liquid-solid technique", Chemical Physics Letters **504**, 1, 62–66 (2011a).

Devami, K., D. Kang, J.-S. Lee and M. Meyyappan, "Synthesis of ZnTe nanostructures by vapor-liquid-solid technique", **504**, 1, 62–66 (2011b).

Du, J., L. Q. Xu, G. F. Zou, L. L. Chai and Y. T. Qian, "Solvothermal synthesis of single crystalline znte nanorod bundles in a mixed solvent of ethylenediamine and hydrazine hydrate", Journal of Crystal Growth **291**, 1, 183–186 (2006).

Escobedo, A., S. Quinones, M. Adame, J. McClure, D. Zubia and G. Brill, "Characterization of smooth cdte(111) films by the conventional close-spaced sublimation technique", Journal of Electronic Materials **39**, 4, 400–409 (2010).

Fan, J., L. Ouyang, X. Liu, D. Ding, J. K. Furdyna, D. J. Smith and Y. H. Zhang, "Growth and material properties of znte on gaas, inp, inas and gasb (001) substrates for electronic and optoelectronic device applications", Journal of Crystal Growth **323**, 1, 127–131 (2011).

Farkas, D., S. Mohanty and J. Monk, "Linear grain growth kinetics and rotation in nanocrystalline ni", Physical review letters **98**, 16, 165502 (2007).

Fasoli, A., A. Colli, S. Hofmann, C. Ducati, J. Robertson and A. Ferrari, "Shape-selective synthesis of ii–vi semiconductor nanowires", physica status solidi (b) **243**, 13, 3301–3305 (2006).

Fischer, A. G., J. N. Carides and J. Dresner, "Preparation and properties of n-type ZnTe", Solid State Communications **2**, 6, 157–159, URL http://www.sciencedirect.com/science/article/pii/0038109864901036 (1964).

Foley, A., B. M. Smyth, T. Puksec, N. Markovska and N. Duic, "A review of developments in technologies and research that have had a direct measurable impact on sustainability considering the Paris agreement on climate change", Renewable and Sustainable Energy Reviews **68**, 835–839, URL http://www.sciencedirect.com/science/article/pii/S136403211630987X (2017).

Fujita, S., S. Arai, F. Itoh and T. Sakaguchi, "Electrical properties and injection luminescence in znse-znte heterojunctions prepared by liquid-phase epitaxy", Journal of Applied Physics **46**, 7, 3070–3075 (1975).

Garcia, J. A., P. Fernandez, A. Remon, J. Piqueras, V. Munoz and R. Triboulet, "Cathodoluminescence and photoluminescence study of plastically deformed znte bulk single crystals", Semiconductor Science and Technology **16**, 5, 289–292 (2001).

Gessert, T. A., W. K. Metzger, P. Dippo, S. E. Asher, R. G. Dhere and M. R. Young, "Dependence of carrier lifetime on Cu-contacting temperature and ZnTe:Cu thickness in CdS/CdTe thin film solar cells", Thin Solid Films **517**, 7, 2370–2373, URL http://www.sciencedirect.com/science/article/pii/S0040609008013758, 00057 (2009).

Ghosh, B., D. Ghosh, S. Hussain, R. Bhar and A. Pal, "Growth of znte films by pulsed laser deposition technique", Journal of Alloys and Compounds **541**, 104–110 (2012).

Goto, H., K. Nosaki, K. Tomioka, S. Hara, K. Hiruma, J. Motohisa and T. Fukui, "Growth of core–shell inp nanowires for photovoltaic application by selective-area metal organic vapor phase epitaxy", Applied Physics Express **2**, 3, 035004 (2009).

Gunshor, R. L., J. Han, G. C. Hua, A. V. Nurmikko and H. Jeon, "Growth issues for blue-green laser diodes", Journal of Crystal Growth **159**, 1-4, 1–10 (1996).

Guo, Y., B. Geng, L. Zhang, F. Zhan and J. You, "Fabrication, characterization, and strong exciton emission of multilayer ZnTe nanowire superstructures", **112**, 51, 20307–20311, URL http://dx.doi.org/10.1021/jp8081497 (2008).

Hochbaum, A. I. and P. Yang, "Semiconductor nanowires for energy conversion", Chemical reviews **110**, 1, 527–546 (2009).

Hu, L. and G. Chen, "Analysis of optical absorption in silicon nanowire arrays for photovoltaic applications", Nano letters **7**, 11, 3249–3252 (2007).

Huo, H. B., L. Dai, C. Liu, L. P. You, W. Q. Yang, R. M. Ma, G. Z. Ran and G. G. Qin, "Electrical properties of Cu doped p-ZnTe nanowires", Nanotechnology **17**, 24, 5912, URL

http://iopscience.iop.org.ezproxy1.lib.asu.edu/0957-4484/17/24/002, 00049 (2006a).

Huo, H. B., L. Dai, D. Y. Xia, G. Z. Ran, L. P. You, B. R. Zhang and G. G. Qin, "Synthesis and optical properties of ZnTe single-crystalline nanowires", Journal of Nanoscience and Nanotechnology **6**, 4, 1182–1184, wOS:000237069200042 (2006b).

Janik, E., P. Dluzewski, S. Kret, A. Presz, H. Kirmse, W. Neumann, W. Zaleszczyk, L. T. Baczewski, A. Petroutchik, E. Dynowska, J. Sadowski, W. Caliebe, G. Karczewski and T. Wojtowicz, "Catalytic growth of ZnTe nanowires by molecular beam epitaxy: structural studies", **18**, 47, 475606, URL http://iopscience.iop.org.ezproxy1.lib.asu.edu/0957-4484/18/47/475606, 00043 (2007).

Jie, J. S., W. J. Zhang, I. Bello, C. S. Lee and S. T. Lee, "One-dimensional ii-vi nanostructures: Synthesis, properties and optoelectronic applications", Nano Today **5**, 4, 313–336 (2010).

Kaminow, I. P. and E. H. Turner, "Electrooptic Light Modulators", Applied Optics **5**, 10, 1612, URL https://www.osapublishing.org/abstract.cfm?URI=ao-5-10-1612 (1966).

Kang, Z., H. Menkara, B. Wagner, C. Summers, R. Durst, Y. Diawara, G. Mednikova and T. Thorson, "Effects of annealing atmosphere on the luminescent efficiency of znte: O phosphors", Journal of luminescence **117**, 2, 156–162 (2006a).

Kang, Z., H. Menkara, B. Wagner, C. Summers, R. Durst, Y. Diawara, G. Mednikova and T. Thorson, "Oxygen-doped znte phosphors for synchrotron x-ray imaging detectors", Journal of electronic materials **35**, 6, 1262–1266 (2006b).

Kayes, B. M., H. A. Atwater and N. S. Lewis, "Comparison of the device physics principles of planar and radial p-n junction nanorod solar cells", Journal of applied physics **97**, 11, 114302 (2005).

Khawaja, E., M. Al-Daous, S. Durrani and M. Al-Kuhaili, "Chemical inhomogeneity in zinc telluride thin films prepared by thermal evaporation", Thin Solid Films **485**, 1, 16–21 (2005).

Kim, S., B. Fisher, H.-J. Eisler and M. Bawendi, "Type-ii quantum dots: Cdte/cdse (core/shell) and cdse/znte (core/shell) heterostructures", Journal of the American Chemical Society **125**, 38, 11466–11467 (2003).

Kong, X. Y. and Z. L. Wang, "Spontaneous polarization-induced nanohelixes, nanosprings, and nanorings of piezoelectric nanobelts", Nano Letters **3**, 12, 1625–1631 (2003).

Kumagai, Y. and M. Kobayashi, "Growth of ZnMgTe/ZnTe Waveguide Structures and Analysis of the Light Polarization with the Electric Field", Japanese Journal of Applied Physics **51**, 2, 02BH06, URL http://stacks.iop.org/1347-4065/51/02BH06 (2012).

Kumar, B. R., B. Hymavathi and T. S. RAOa, "Investigations on physical properties of nanostructured znte thin films prepared by dc reactive magnetron sputtering", Chalcogenide Letters **11**, 10, 509–517 (2014).

Larach, S., R. E. Shrader and C. F. Stocker, "Anomalous variation of band gap with composition in zinc sulfo- and seleno-tellurides", **108**, 3, 587–589, URL http://link.aps.org/doi/10.1103/PhysRev.108.587, 00167 (1957).

Leschkies, K. S., R. Divakar, J. Basu, E. Enache-Pommer, J. E. Boercker, C. B. Carter, U. R. Kortshagen, D. J. Norris and E. S. Aydil, "Photosensitization of zno nanowires with cdse quantum dots for photovoltaic devices", Nano Letters **7**, 6, 1793–1798 (2007).

Lévy-Clément, C., R. Tena-Zaera, M. A. Ryan, A. Katty and G. Hodes, "Cdse-sensitized p-cuscn/nanowire n-zno heterojunctions", Advanced Materials **17**, 12, 1512–1515 (2005).

Li, L., Y. Yang, X. Huang, G. Li and L. Zhang, "Fabrication and characterization of single-crystalline ZnTe nanowire arrays", **109**, 25, 12394–12398, URL http://dx.doi.org/10.1021/jp0511855 (2005).

Li, S., Y. Jiang, D. Wu, B. Wang, Y. Zhang, J. Li, X. Liu, H. Zhong, L. Chen and J. Jie, "Structure and electrical properties of p-type twin znte nanowires", Applied Physics A: Materials Science & Processing **102**, 2, 469–475 (2011a).

Li, S., Y. Jiang, D. Wu, B. Wang, Y. Zhang, J. Li, X. Liu, H. Zhong, L. Chen and J. Jie, "Structure and electrical properties of p-type twin ZnTe nanowires", **102**, 2, 469–475 (2011b).

Li, S., Y. Jiang, D. Wu, L. Wang, H. Zhong, B. Wu, X. Lan, Y. Yu, Z. Wang and J. Jie, "Enhanced p-Type Conductivity of ZnTe Nanoribbons by Nitrogen Doping", The Journal of Physical Chemistry C **114**, 17, 7980–7985, URL http://dx.doi.org/10.1021/jp911873j, 00032 (2010a).

Li, S., Y. Jiang, D. Wu, L. Wang, H. Zhong, B. Wu, X. Lan, Y. Yu, Z. Wang and J. Jie, "Enhanced p-type conductivity of znte nanoribbons by nitrogen doping", The Journal of Physical Chemistry C **114**, 17, 7980–7985 (2010b).

Li, Z., J. Salfi, C. D. Souza, P. Sun, S. V. Nair and H. E. Ruda, "Room temperature single nanowire ZnTe photoconductors grown by metal-organic chemical vapor deposition", Applied Physics Letters **97**, 6, 063510, 00013 (2010c).

Lieber, C. M. and Z. L. Wang, "Functional nanowires", **32**, 2, 99–108, URL http://journals.cambridge.org/article$_S$0883769400007053(2007).

Liu, Z., G. Chen, B. Liang, G. Yu, H. Huang, D. Chen and G. Shen, "Fabrication of high-quality ZnTe nanowires toward high-performance rigid/flexible visible-light photodetectors", **21**, 6, 7799–7810, URL http://www.opticsexpress.org/abstract.cfm?URI=oe-21-6-7799, 00010 (2013a).

Liu, Z., G. Chen, B. Liang, G. Yu, H. T. Huang, D. Chen and G. Z. Shen, "Fabrication of high-quality znte nanowires toward high-performance rigid/flexible visible-light photodetectors", Optics Express **21**, 6, 7799–7810 (2013b).

Marfaing, Y., "Fundamental studies on compensation mechanisms in II-VI compounds", Journal of Crystal Growth **161**, 1-4, 205–213, URL `http://www.sciencedirect.com/science/article/pii/0022024895006419`, 00040 (1996).

Meng, Q., C. Jiang and S. X. Mao, "Temperature-dependent growth of zinc-blende-structured znte nanostructures", Journal of Crystal Growth **310**, 20, 4481–4486 (2008a).

Meng, Q., C. Jiang and S. X. Mao, "Temperature-dependent growth of zinc-blende-structured ZnTe nanostructures", **310**, 20, 4481–4486, URL `http://www.sciencedirect.com/science/article/pii/S0022024808006672`, 00045 (2008b).

Meng, Q. F., C. B. Jiang and S. X. Mao, "Ohmic contacts and photoconductivity of individual ZnTe nanowires", Applied Physics Letters **94**, 4, 043111 (2009).

Moon, Y.-T., D.-J. Kim, K.-M. Song, C.-J. Choi, S.-H. Han, T.-Y. Seong and S.-J. Park, "Effects of thermal and hydrogen treatment on indium segregation in InGaN/GaN multiple quantum wells", Journal of Applied Physics **89**, 11, 6514 (2001).

Mote, V., Y. Purushotham and B. Dole, "Williamson-hall analysis in estimation of lattice strain in nanometer-sized zno particles", Journal of theoretical and applied physics **6**, 1, 6 (2012).

Nam, S., Y.-M. Yu, J. Rhee, O. Byungsung, K.-S. Lee, Y. D. Choi, J. W. Lee and S. Sakakibara, "Gaas substrate thermal preheating effect exerted on znte epilayer", Journal of crystal growth **212**, 3, 416–422 (2000).

Nieto, A., L. Huang, Y.-H. Han and J. M. Schoenung, "Sintering behavior of spark plasma sintered alumina with graphene nanoplatelet reinforcement", Ceramics International **41**, 4, 5926–5936 (2015).

Opanasyuk, A. S., D. I. Kurbatov, V. V. Kosyak, S. I. Kshniakina and S. N. Danilchenko, "Characteristics of structure formation in zinc and cadmium chalcogenide films deposited on nonorienting substrates", Crystallography Reports **57**, 7, 927–933 (2012).

Osamura, K., S. Naka and Y. Murakami, "Preparation and optical properties of ga(1-x) in x n thin films", Journal of Applied Physics **46**, 8, 3432–3437 (1975).

Ozgur, U., Y. I. Alivov, C. Liu, A. Teke, M. A. Reshchikov, S. Dogan, V. Avrutin, S.-J. Cho and H. Morkoc, "A comprehensive review of ZnO materials and devices", Journal of Applied Physics **98**, 4, 041301 (2005).

Pak, S. W., J. Suh, D. U. Lee and E. K. Kim, "Growth of znte: O thin films by oxygen-plasma-assisted pulsed laser deposition", Japanese Journal of Applied Physics **51**, 1S, 01AD04 (2012).

Park, J.-H., H.-J. Choi, Y.-J. Choi, S.-H. Sohn and J.-G. Park, "Ultrawide ZnO nanosheets", Journal of Materials Chemistry **14**, 1, 35–36, 00176 (2004a).

Park, J.-H., H.-J. Choi and J.-G. Park, "Scaffolding and filling process: A new type of 2d crystal growth", Journal of Crystal Growth **263**, 1, 237–242 (2004b).

Park, J.-H., H.-J. Choi and J.-G. Park, "Scaffolding and filling process: a new type of 2d crystal growth", **263**, 1, 237–242 (2004c).

Park, J.-H., Y.-J. Choi and J.-G. Park, "Synthesis of ZnO nanowires and nanosheets by an O2-assisted carbothermal reduction process", Journal of Crystal Growth **280**, 1-2, 161–167, URL `http://www.sciencedirect.com/science/article/pii/S0022024805003283` (2005).

Pelekanos, N., J. Ding, Q. Fu, A. V. Nurmikko, S. M. Durbin, M. Kobayashi and R. L. Gunshor, "Hot-exciton luminescence in ZnTe/MnTe quantum wells", Physical Review B **43**, 11, 9354–9357, URL `http://link.aps.org/doi/10.1103/PhysRevB.43.9354` (1991).

Ramgir, N. S., Y. Yang and M. Zacharias, "Nanowire-based sensors", **6**, 16, 1705–1722, 113 (2010).

Rao, G. K., K. V. Bangera and G. Shivakumar, "Studies on the photoconductivity of vacuum deposited znte thin films", Materials Research Bulletin **45**, 10, 1357–1360 (2010).

Rao, G. K., K. V. Bangera and G. K. Shivakumar, "The effect of substrate temperature on the structural, optical and electrical properties of vacuum deposited znte thin films", Vacuum **83**, 12, 1485–1488 (2009).

Rathod, J., H. Patel, K. Patel and V. Pathak, "Properties of thin-film zinc telluride prepared by thermal evaporation", in "Aip Conference Proceedings", vol. 1393, pp. 121–122 (AIP, 2011).

Reiss, P., M. Protiere and L. Li, "Core/shell semiconductor nanocrystals", Small **5**, 2, 154–168 (2009).

Rioux, D., D. W. Niles and H. Hochst, "ZnTe: A potential interlayer to form low resistance back contacts in CdS/CdTe solar cells", Journal of Applied Physics **73**, 12, 8381–8385, 00093 (1993).

Rose, A., *Concepts in photoconductivity and allied problems*, Interscience tracts on physics and astronomy, 19 (Interscience Publishers, New York, 1963), 01609.

Ruda, H. E., "Compensation and transport characteristics of n-ZnTe", **24**, 7, 1158, URL http://iopscience.iop.org.ezproxy1.lib.asu.edu/0022-3727/24/7/021, 00011 (1991).

Salem, A. M., T. M. Dahy and Y. A. El-Gendy, "Thickness dependence of optical parameters for znte thin films deposited by electron beam gun evaporation technique", Physica B-Condensed Matter **403**, 18, 3027–3033 (2008).

Schrier, J., D. O. Demchenko and A. P. Alivisatos, "Optical properties of zno/zns and zno/znte heterostructures for photovoltaic applications", Nano letters **7**, 8, 2377–2382 (2007).

Shaaban, E. R., I. Kansal, S. Mohamed and J. M. Ferreira, "Microstructural parameters and optical constants of znte thin films with various thicknesses", Physica B: Condensed matter **404**, 20, 3571–3576 (2009).

Shaban, E., M. Ahmad, E. A. Wahab, H. S. Hassan and A. Aboraia, "Structural and optical properties of varies thickness of znte nanoparticle", ANGLISTICUM. Journal of the Association for Anglo-American Studies **3** (2016).

Shan, C. X., X. W. Fan, J. Y. Zhang, Z. Z. Zhang, X. H. Wang, J. G. Ma, Y. M. Lu, Y. C. Liu, D. Z. Shen, X. G. Kong and G. Z. Zhong, "Structural and luminescent properties of znte film grown on silicon by metalorganic chemical vapor deposition", Journal of Vacuum Science Technology a-Vacuum Surfaces and Films **20**, 6, 1886–1890 (2002).

Soci, C., A. Zhang, B. Xiang, S. A. Dayeh, D. Aplin, J. Park, X. Bao, Y.-H. Lo and D. Wang, "Zno nanowire uv photodetectors with high internal gain", Nano letters **7**, 4, 1003–1009 (2007a).

Soci, C., A. Zhang, B. Xiang, S. A. Dayeh, D. P. R. Aplin, J. Park, X. Y. Bao, Y. H. Lo and D. Wang, "ZnO nanowire UV photodetectors with high internal gain", **7**, 4, 1003–1009, URL http://dx.doi.org/10.1021/nl070111x, 01120 (2007b).

Spath, B., J. Fritsche, F. Sauberlich, A. Klein and W. Jaegermann, "Studies of sputtered znte films as interlayer for the cdte thin film solar cell", Thin Solid Films **480**, 204–207 (2005a).

Spath, B., J. Fritsche, F. Sauberlich, A. Klein and W. Jaegermann, "Studies of sputtered ZnTe films as interlayer for the CdTe thin film solar cell", Thin Solid Films **480-481**, 204–207, URL http://www.sciencedirect.com/science/article/pii/S0040609004016542, 00040 (2005b).

Syed Basheer Ahamed, M., V. Nagarethinam, A. Thayumanavan, K. Murali, C. Sanjeeviraja and M. Jayachandran, "Structural, optical, electrical and morphological properties of znte films deposited by electron beam evaporation", Journal of Materials Science: Materials in Electronics **21**, 12, 1229–1234 (2010).

Sze, S. M. and K. K. Ng, *Physics of Semiconductor Devices* (Wiley-Interscience, Hoboken, N.J, 2006), 3 edition edn., 39840.

Tak, Y., S. J. Hong, J. S. Lee and K. Yong, "Fabrication of zno/cds core/shell nanowire arrays for efficient solar energy conversion", Journal of Materials Chemistry **19**, 33, 5945–5951 (2009).

Tanaka, T., K. Saito, M. Nishio, Q. X. Guo and H. Ogawa, "Enhanced light output from znte light emitting diodes by utilizing thin film structure", Applied Physics Express **2**, 12 (2009a).

Tanaka, T., K. Saito, M. Nishio, Q. X. Guo and H. Ogawa, "Fabrication of a znte light emitting diode by al thermal diffusion into a p-znte epitaxial layer on a p-znmgte substrate", Journal of Materials Science-Materials in Electronics **20**, 505–509 (2009b).

Tian, B., T. J. Kempa and C. M. Lieber, "Single nanowire photovoltaics", **38**, 1, 16–24, WOS:000261768900002 (2009).

Tian, B., X. Zheng, T. J. Kempa, Y. Fang, N. Yu, G. Yu, J. Huang and C. M. Lieber, "Coaxial silicon nanowires as solar cells and nanoelectronic power sources", **449**, 7164, 885–889, 01899 (2007).

Torchynska, T. and G. Polupan, "Iii-v material solar cells for space application", Semiconductor Physics Quantum Electronics & Optoelectronics (2002).

Utama, M. I. B., M. de la Mata, Q. Zhang, C. Magen, J. Arbiol and Q. Xiong, "The growth of ultralong znte micro/nanostructures: The influence of polarity and twin direction on the morphogenesis of nanobelts and nanosheets", Cryst. Growth Des **13**, 6, 2590–2596 (2013a).

Utama, M. I. B., M. de la Mata, Q. Zhang, C. Magen, J. Arbiol and Q. Xiong, "The Growth of Ultralong ZnTe Micro/Nanostructures: The Influence of Polarity and Twin Direction on the Morphogenesis of Nanobelts and Nanosheets", Crystal Growth & Design **13**, 6, 2590–2596, 00002 WOS:000320153400041 (2013b).

Van de Krol, R., Y. Liang and J. Schoonman, "Solar hydrogen production with nanostructured metal oxides", Journal of Materials Chemistry **18**, 20, 2311–2320 (2008).

Wang, K., J. Chen, Z. Zeng, J. Tarr, W. Zhou, Y. Zhang, Y. Yan, C. Jiang, J. Pern and A. Mascarenhas, "Synthesis and photovoltaic effect of vertically aligned zno/zns core/shell nanowire arrays", Applied Physics Letters **96**, 12, 123105 (2010).

Wang, K., J. Chen, W. Zhou, Y. Zhang, Y. Yan, J. Pern and A. Mascarenhas, "Direct growth of highly mismatched type ii zno/znse core/shell nanowire arrays on transparent conducting oxide substrates for solar cell applications", Advanced Materials **20**, 17, 3248–3253 (2008).

Wang, W., A. S. Lin and J. D. Phillips, "Intermediate-band photovoltaic solar cell based on znte: O", Applied Physics Letters **95**, 1, 011103 (2009).

Wang, X., J. Song and Z. L. Wang, "Nanowire and nanobelt arrays of zinc oxide from synthesis to properties and to novel devices", Journal of Materials Chemistry **17**, 8, 711–720 (2007).

Wang, Z., "Nanopiezotronics", Advanced Materials **19**, 6, 889–892, URL http://doi.wiley.com/10.1002/adma.200602918 (2007).

Wang, Z. L., "ZnO nanowire and nanobelt platform for nanotechnology", **64**, 3, 33–71, URL http://www.sciencedirect.com/science/article/pii/S0927796X09000229, 458 (2009).

Wu, D., Y. Jiang, X. Yao, Y. Chang, Y. Zhang, Y. Yu, Z. Zhu, Y. Zhang, X. Lan and H. Zhong, "Construction of crossed heterojunctions from p-ZnTe and n-CdSe nanoribbons and their photoresponse properties", Journal of Materials Chemistry C **2**, 32, 6547–6553, 00000 (2014).

Wu, D., Y. Jiang, Y. Zhang, J. Li, Y. Yu, Y. Zhang, Z. Zhu, L. Wang, C. Wu, L. Luo and J. Jie, "Device structure-dependent field-effect and photoresponse performances of p-type ZnTe:Sb nanoribbons", Journal of Materials Chemistry **22**, 13, 6206–6212 (2012).

Xu, M., K. Gao, J. Wu, H. Cai, Y. Yuan, S. Prucnal, R. Hübner, W. Skorupa, M. Helm and S. Zhou, "Polycrystalline znte thin film on silicon synthesized by pulsed laser deposition and subsequent pulsed laser melting", Materials Research Express **3**, 3, 036403 (2016).

Xu, W., A. Chin, L. Ye, C. Z. Ning and H. Yu, "Charge transport and trap characterization in individual GaSb nanowires", **111**, 10, 104515 (2012).

Xue, D. and S. Zhang, "Bond-Charge Calculation of Electro-Optic Coefficients of Diatomic Crystals", Journal of Solid State Chemistry **128**, 1, 17–20, URL http://www.sciencedirect.com/science/article/pii/S0022459696971285 (1997).

Ye, J., K. Zhen, S. Gu, F. Wang, H. H. Tan and C. Jagadish, "Formation of intermediate band in znte: O highly mismatched alloy synthesized by ion implantation", in "Optoelectronic And Microelectronic Materials & Devices (commad), 2014 Conference On", pp. 259–261 (IEEE, 2014).

Yim, J. W., D. Chen, G. F. Brown and J. Wu, "Synthesis and ex situ doping of znte and znse nanostructures with extreme aspect ratios", Nano Research **2**, 12, 931–937 (2009).

Yong, K.-T., Y. Sahoo, H. Zeng, M. T. Swihart, J. R. Minter and P. N. Prasad, "Formation of ZnTe nanowires by oriented attachment", **19**, 17, 4108–4110, URL http://dx.doi.org/10.1021/cm0709774, 59 (2007).

You-Wen, Y., L. Liang, Y. Min, W. Yu-Cheng, X. Ting and L. Guang-Hai, "Electrochemical deposition and properties of ZnTe nanowire array", **24**, 10, 2973, URL http://iopscience.iop.org.ezproxy1.lib.asu.edu/0256-307X/24/10/072, 00006 (2007).

Young, S.-J. and Y.-H. Liu, "Enhanced field emission properties of two-dimensional ZnO nanosheets under UV illumination", **21**, 4, 1–4 (2015).

Yu, H., E. A. Azhar, T. Belagodu, S. Lim and S. Dey, "ZnO nanowire based visible-transparent ultraviolet detectors on polymer substrates", **111**, 10, 102806 (2012).

Zhang, H., J. Huang, X. Zhou and X. Zhong, "Single-crystal bi2s3 nanosheets growing via attachment and recrystallization of nanorods", **50**, 16, 7729–7734, URL http://dx.doi.org/10.1021/ic201332n, 00017 (2011).

Zhang, J., P.-C. Chen, G. Shen, J. He, A. Kumbhar, C. Zhou and J. Fang, "p-type field-effect transistors of single-crystal zinc telluride nanobelts", **47**, 49, 9469–9471, 24 (2008a).

Zhang, J., P.-C. Chen, G. Shen, J. He, A. Kumbhar, C. Zhou and J. Fang, "P-type field-effect transistors of single-crystal zinc telluride nanobelts", Angewandte Chemie International Edition **47**, 49, 9469–9471 (2008b).

Zhang, Q., J. Zhang, M. Utama, B. d. Peng, M. De La Mata, J. Arbiol and Q. Xiong, "Exciton-phonon coupling in individual znte nanorods studied by resonant raman spectroscopy", Physical Review B **85**, 8, 085418 (2012).

Zhang, Y., J. Pern, A. Mascarenhas and W. Zhou, "Searching for optimal solar-cell architectures", SPIE Newsroom (2008c).

Zheng, J., Z. Wu, W. Yang, S. Li and J. Kang, "Growth and characterization of type ii zno/znse core/shell nanowire arrays", Journal of Materials Research **25**, 7, 1272–1277 (2010).

Zhou, L., H. Zhang and D. J. Srolovitz, "A size effect in grain boundary migration: A molecular dynamics study of bicrystal thin films", Acta materialia **53**, 20, 5273–5279 (2005).

Zhou, L. Q., C. Chen, H. Jia, C. Ling, D. Banerjee, J. D. Phillips and Y. Wang, "Oxygen incorporation in znteo alloys via molecular beam epitaxy", Journal of electronic materials **43**, 4, 889 (2014).

Zielony, E., E. Placzek-Popko, P. Nowakowski, Z. Gumienny, A. Suchocki and G. Karczewski, "Electro-optical characterization of ti/au znte schottky diodes with cdte quantum dots", Materials Chemistry and Physics **134**, 23, 821–828, URL http://www.sciencedirect.com/science/article/pii/S0254058412003252, 00002 (2012).